Electronic Supplementary Information (ESI)

Utility of redox-active ligands for reversible multi-electron transfer in uranyl(VI) complexes

Tomoyuki Takeyama, *[a] Satoru Tsushima,[b,c] Koichiro Takao*,[a]

AUTHOR ADDRESS

[a] Laboratory for Zero-Carbon Energy, Institute of Innovative Research, Tokyo Institute of Technology 2-12-1 N1-32, O-okayama, Meguro-ku, 152-8550 Tokyo, Japan

[b] Institute of Resource Ecology, Helmholtz-Zentrum Dresden-Rossendorf (HZDR), Bautzner Landstraße 400, 01328 Dresden, Germany

[c] International Research Frontiers Initiative (IRFI), Institute of Innovative Research, Tokyo Institute of Technology, 2-12-1, O-okayama, Meguro-ku, 152-8550 Tokyo, Japan
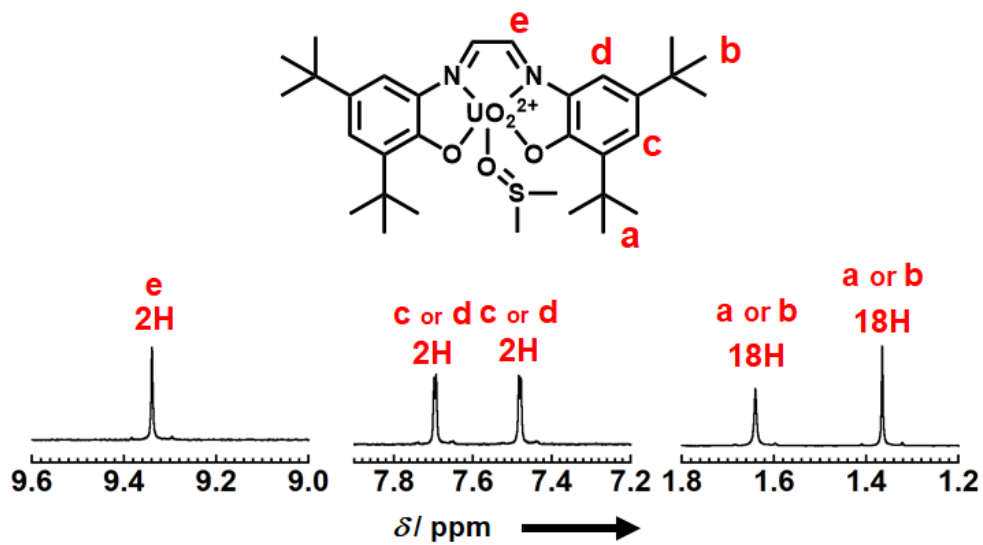
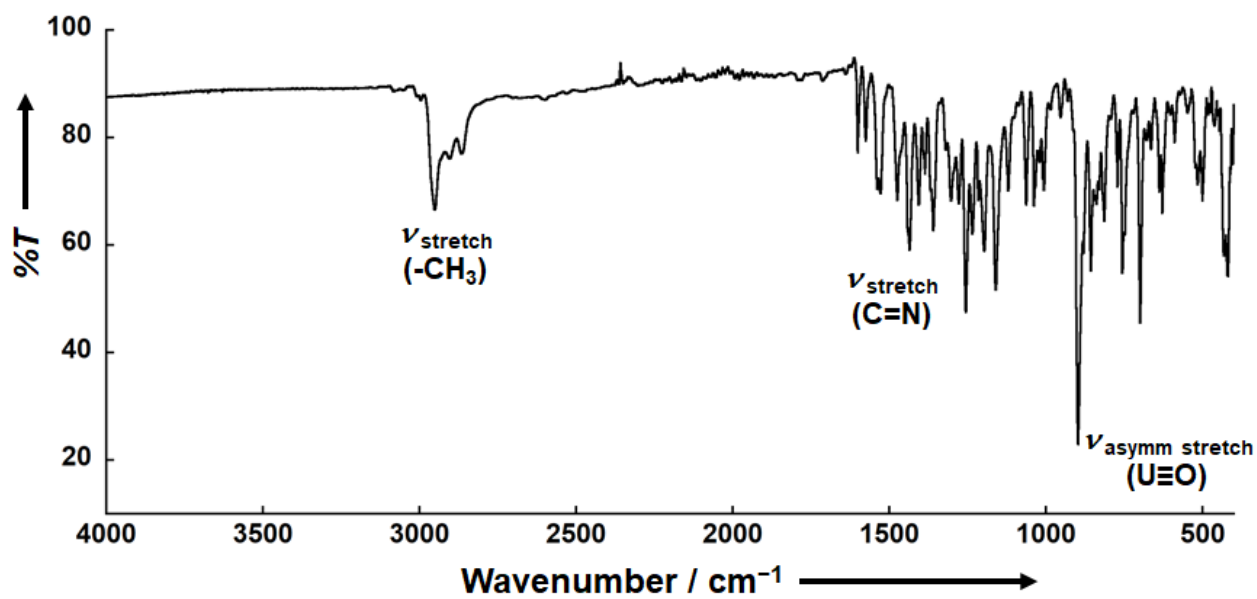**Figure S1.** ^{1}H NMR spectra of [U^{VI}O$_2$(L1)DMSO] in DMSO-d_6.
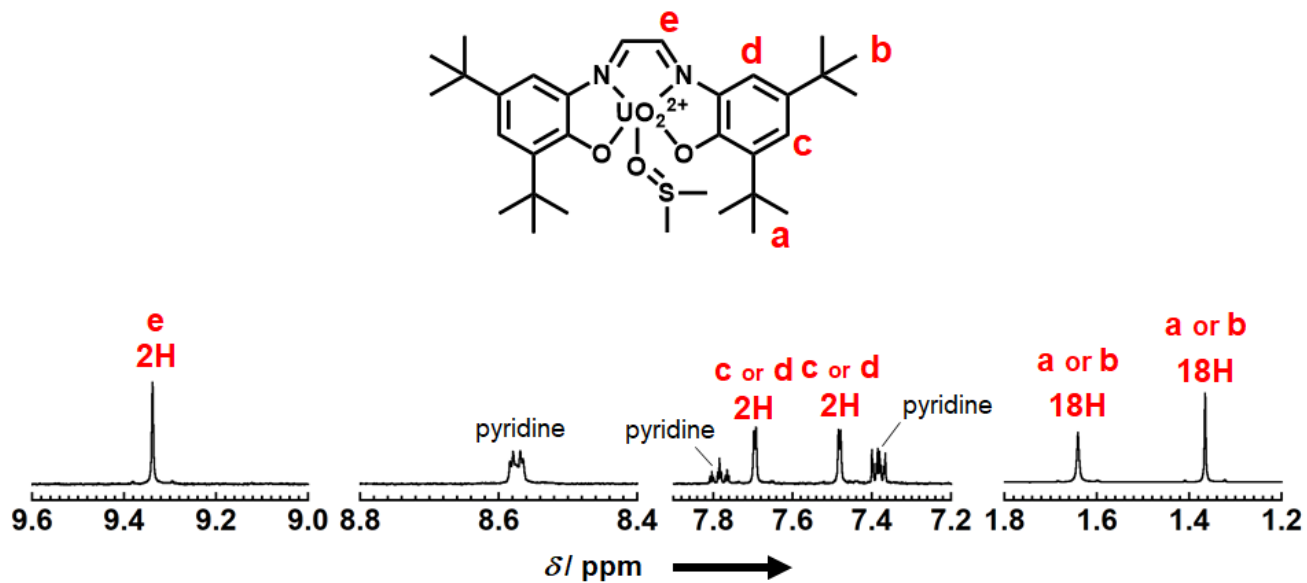

Figure S2. IR spectra of [U^{VI}O$_2$(L1)DMSO].

Figure S3. ^{1}H NMR spectra of the DMSO-d_6 solution dissolving [U^{VI}O$_2$(L1)C$_5$H$_5$N].
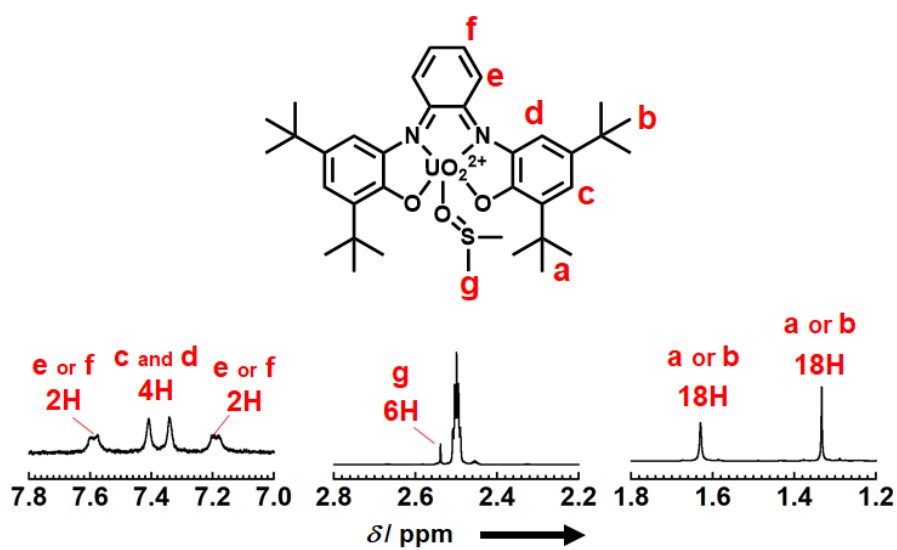

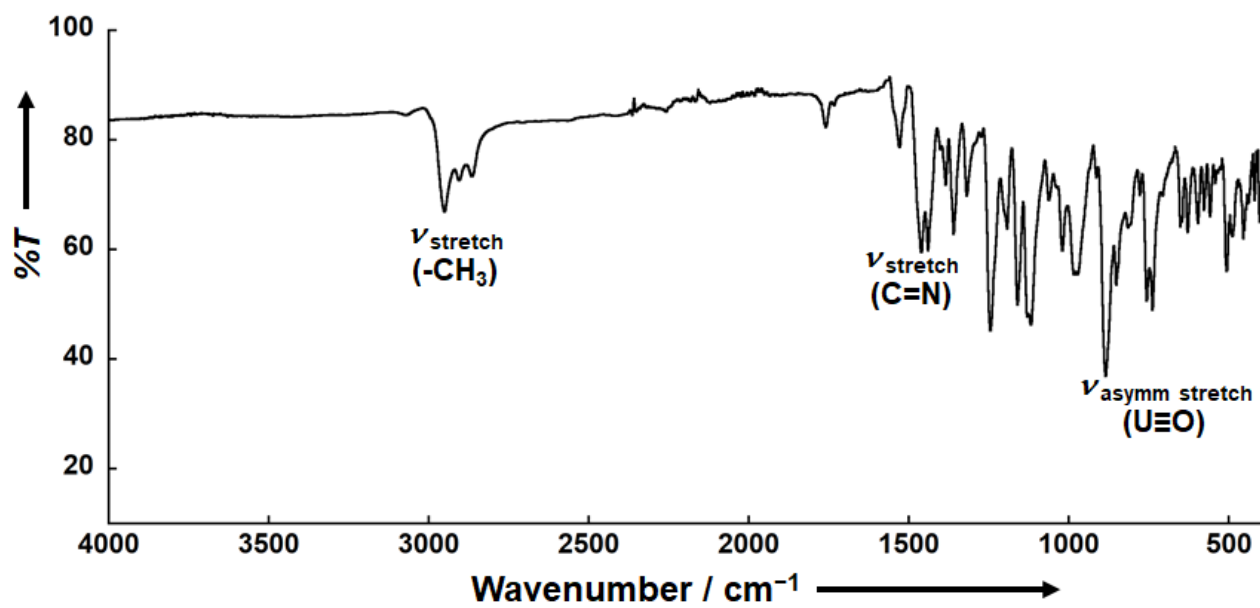**Figure S4.** ^{1}H NMR spectra of [U^{VI}O$_2$(L2)DMSO] in DMSO-d_6.

Figure S5. IR spectra of [U^{VI}O$_2$(L2)DMSO].

Crystal structure of [$U^{VI}O_2$(L2)DMSO]·(DMSO)$_{0.5}$

The crystal structure analysis of [$U^{VI}O_2$(L2)DMSO]·(DMSO)$_{0.5}$ was performed. The obtained molecular structures of [$U^{VI}O_2$(L2)DMSO] are shown in Figure S6. And crystallographic data is listed below.

Crystallographic data for [$U^{VI}O_2$(L2)DMSO]·(DMSO)$_{0.5}$: Fw =899.93, 0.15 × 0.05 × 0.02 mm^3, orthorhombic, P21212, a = 28.7510(8) Å, b = 31.6909(9) Å, c = 9.4393(2) Å, V = 8600.6(4) Å^3 , Z = 8, T = 93 K, D_{calcd} = 1.390 g/cm^3, μ(Mo $K\alpha$) = 3.886 mm^{-1}, GOF = 1.016, R_1(I > 2σ) = 0.0786, wR_2(all) = 0.1812.
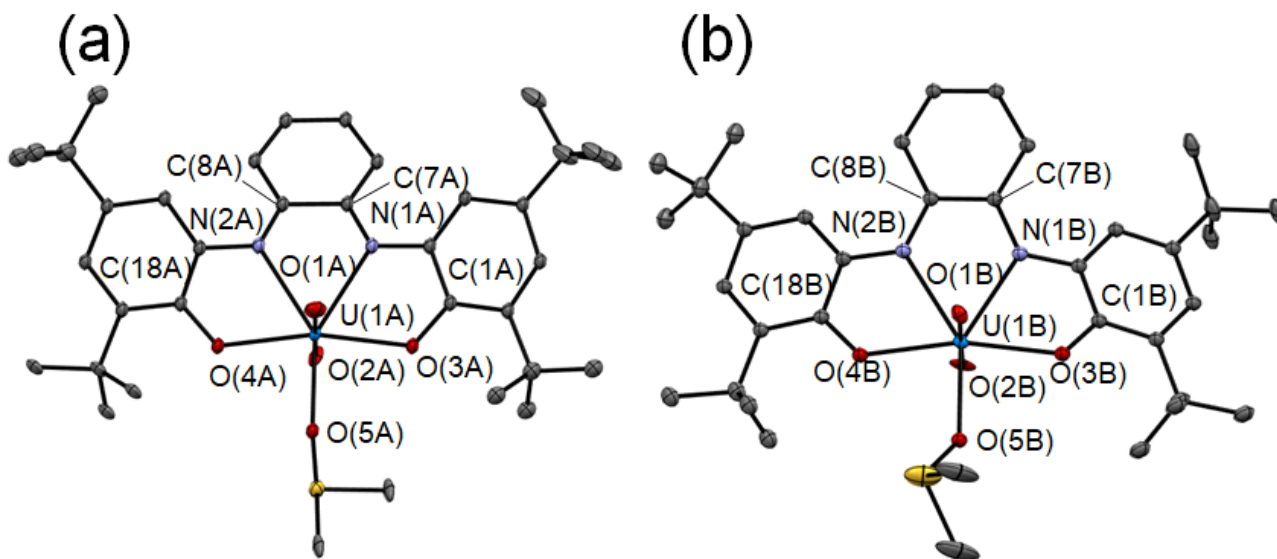

Figure S6. ORTEP views of [$U^{VI}O_2$(L2)DMSO]. Ellipsoids are at 50% probability. Hydrogen atoms and solvent molecules were omitted by clarify. Disordered atoms are also represented.

The molecular structures of [$U^{VI}O_2$(L2)DMSO] are clearly determined, however, high quality of diffraction data was not obtained, because single crystals of [$U^{VI}O_2$(L2)DMSO]·(DMSO)$_{0.5}$ are poorly diffracting needle-like crystals. In spite of many trials for recrystallization and SCXRD experiments, many Alert level A and B are remained by check CIF report of International Union of Crystallography, as described below.

PLAT971_ALERT_2_A Check Calcd Resid. Dens. 1.53Ang From C9B 5.20 eA-3

PLAT971_ALERT_2_A Check Calcd Resid. Dens. 1.42Ang From C9A 3.95 eA-3

PLAT342_ALERT_3_B Low Bond Precision on C-C Bonds...................0.02185 Ang.

PLAT971_ALERT_2_B Check Calcd Resid. Dens. 0.83Ang From C17B 3.15 eA-3

PLAT971_ALERT_2_B Check Calcd Resid. Dens. 1.71Ang From C34A 2.84 eA-3

PLAT971_ALERT_2_B Check Calcd Resid. Dens. 1.52Ang From C2A 2.71 eA-3

PLAT971_ALERT_2_B Check Calcd Resid. Dens. 1.60Ang From C22B 2.57 eA-3

PLAT972_ALERT_2_B Check Calcd Resid. Dens. 1.48Ang From S2 -2.82 eA-3

PLAT972_ALERT_2_B Check Calcd Resid. Dens. 2.20Ang From C10B -2.76 eA-3

PLAT972_ALERT_2_B Check Calcd Resid. Dens. 0.89Ang From U1A -2.51 eA-3

Table S1. Selected bond lengths (Å) of crystal structures of $[U^{VI}O_2(L2)DMSO]\cdot(DMSO)_{0.5}$.

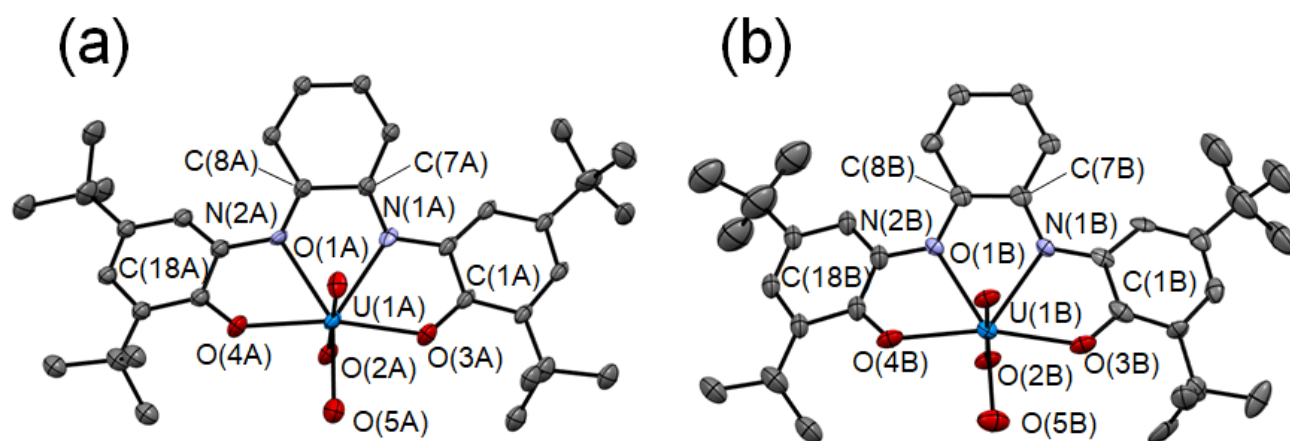| $[U^{VI}O_2(L2)DMSO]\cdot(DMSO)_{0.5}$	
U(1)−O(1)	1.77(1)
	1.78(1)
U(1)−O(2)	1.79(1)
	1.79(1)
U(1)−O(3)	2.273(9)
	2.29(1)
U(1)−O(4)	2.277(9)
	2.30(1)
U(1)−N(1)	2.50(1)
	2.52(1)
U(1)−N(2)	2.52(1)
	2.51(1)
U(1)−O(5)	2.34(1)
	2.35(1)
C(7)−N(1)	1.34(2)
	1.34(2)
C(8)−N(2)	1.31(2)
	1.35(2)
C(1)−O(3)	1.33(2)
	1.33(2)
C(18)−O(4)	1.31(2)
	1.34(1)

Figure S7. ORTEP views of $[U^{VI}O_2(L2)H_2O]$. Ellipsoids are at 50% probability. Hydrogen atoms and solvent molecules were omitted by clarify. Disordered atoms are also represented.

Table S2. Selected bond angles (°) in [$U^{VI}O_2$(L1)C_5H_5N], [$U^{VI}O_2$(L2)H_2O] and [$U^{VI}O_2$(L3)].

[$U^{VI}O_2$(L1)C_5H_5N]		[$U^{VI}O_2$(L2)H_2O]		[$U^{VI}O_2$(L3)]	
∠O(3)−U(1)−N(1)	65.5(3)	∠O(3)−U(1)−N(1)	65.4(3), 65.7(3)	∠O(3)−U(1)−N(1)	65.4(1)
∠N(1)−U(1)−N(2)	62.6(3)	∠N(1)−U(1)−N(2)	61.6(3), 62.9(3)	∠N(1)−U(1)−N(2)	63.2(1)
∠O(4)−U(1)−N(2)	64.8(3)	∠O(4)−U(1)−N(2)	65.5(3), 64.8(3)	∠N(2)−U(1)−N(3)	62.9(1)
∠O(3)−U(1)−N(3)	86.9(3)	∠O(3)−U(1)−O(5)	83.1(3), 77.9(3)	∠N(3)−U(1)−O(4)	65.0(1)
∠O(4)−U(1)−N(3)	80.3(3)	∠O(4)−U(1)−O(5)	84.9(3), 89.1(3)	∠O(3)−U(1)−O(4)	103.6(2)
∠O(1)−U(1)−O(3)	90.6(3)	∠O(1)−U(1)−O(3)	92.2(3), 91.9(3)	∠O(1)−U(1)−O(3)	91.1(2)
∠O(1)−U(1)−N(1)	87.4(3)	∠O(1)−U(1)−N(1)	84.2(3), 88.4(3)	∠O(1)−U(1)−N(1)	85.9(2)
∠O(1)−U(1)−N(2)	87.0(3)	∠O(1)−U(1)−N(2)	89.4(3), 90.4(3)	∠O(1)−U(1)−N(2)	87.7(2)
∠O(1)−U(1)−O(4)	90.6(3)	∠O(1)−U(1)−O(4)	90.2(3), 92.7(3)	∠O(1)−U(1)−N(3)	90.1(2)
∠O(1)−U(1)−N(3)	86.7(3)	∠O(1)−U(1)−O(5)	88.6(3), 86.2(3)	∠O(1)−U(1)−O(4)	90.7(2)
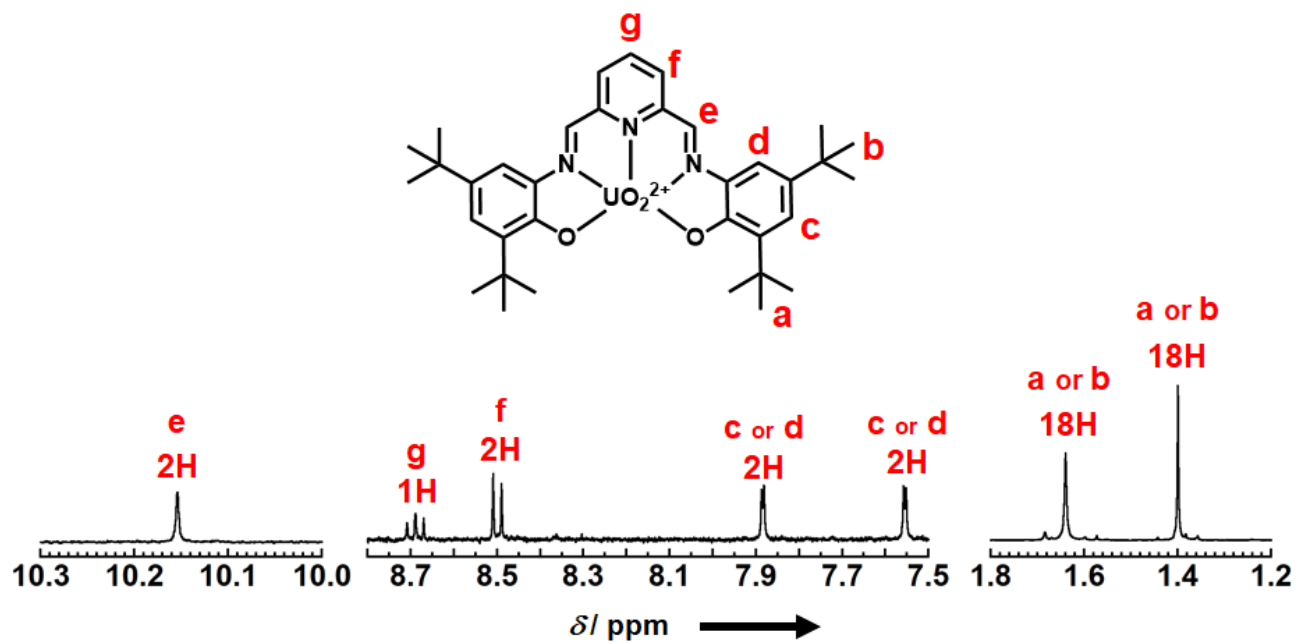
Figure S8. ^{1}H NMR spectra of [U^{VI}O$_2$(L3)] in DMSO-d_6.
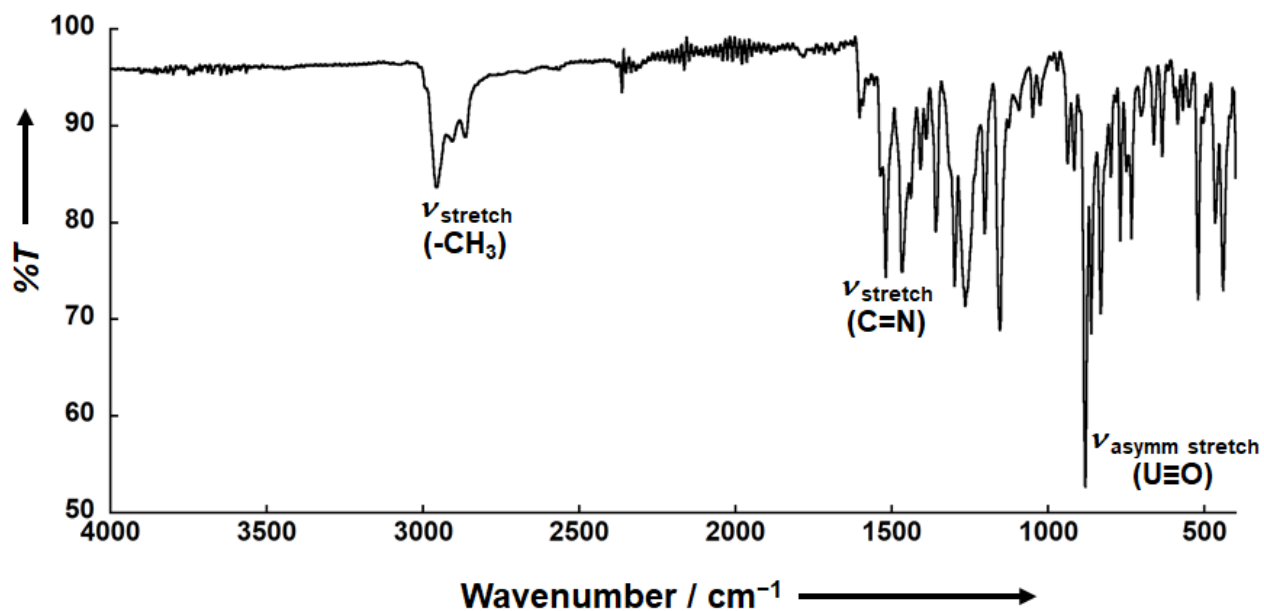
Figure S9. IR spectra of [U^{VI}O$_2$(L3)].
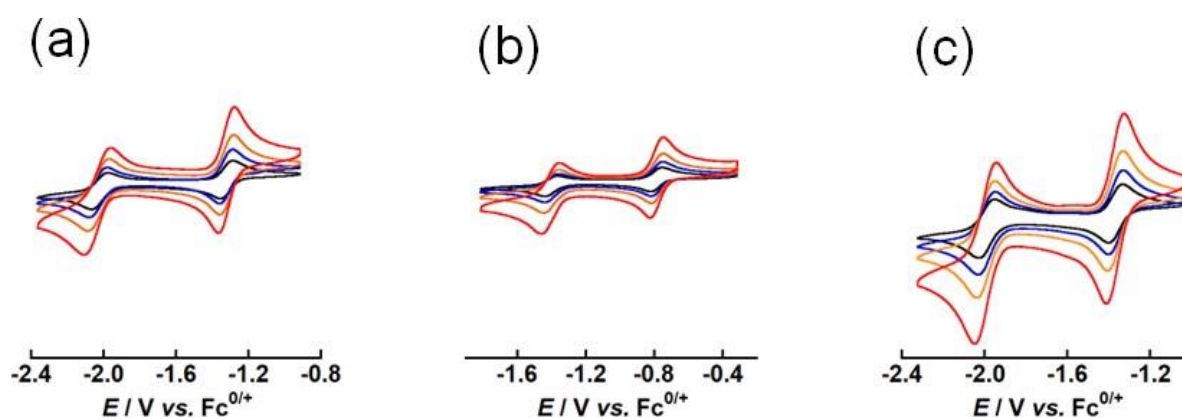
Figure S10. Cyclic voltammograms (CV) for $[U^{VI}O_2(Lx)DMSO_y]$ ($x = 1\text{-}3$, $y = 0\text{-}1$). in DMSO at 295 K. $[U^{VI}O_2(L1)DMSO]$ (a), $[U^{VI}O_2(L2)DMSO]$ (b), and $[U^{VI}O_2(L3)]$ (c). Concentration of the complex was adjusted to 0.50 mM for $[U^{VI}O_2(L1)DMSO]$ and $[U^{VI}O_2(L2)DMSO]$ and 1.00 mM for $[U^{VI}O_2(L3)]$. Tetra-*n*-butylammonium perchlorate (0.1 M) was used as a supporting electrolyte. Potentials in the figures show the relative values to that of the $Fc^{0/+}$ redox couple. Scan rates are 50 mV·s^{-1} (black), 100 mV·s^{-1} (blue), 200 mV·s^{-1} (orange) and 500 mV·s^{-1} (red).

Table S3. Electrochemical data of [U^{VI}O_2(L1)DMSO] in DMSO containing 0.1 M *tetra-n-*butylammonium perchlorate at 295 K. Potentials show the relative values to that of the Fc^{0/+} redox couple.

Scan rate	$E_{pc,1}$ / V	$E_{pa,1}$ / V	E_1°' / V	$\Delta E_{p,1}$ / V	$E_{pc,2}$ / V	$E_{pa,2}$ / V	E_2°' / V	$\Delta E_{p,2}$ / V
50 mV·s⁻¹	−1.35	−1.29	−1.32	0.06	−2.06	−1.98	−2.02	0.08
100 mV·s⁻¹	−1.36	−1.29	−1.33	0.07	−2.08	−1.98	−2.03	0.10
200 mV·s⁻¹	−1.36	−1.28	−1.32	0.08	−2.09	−1.97	−2.03	0.12
500 mV·s⁻¹	−1.37	−1.28	−1.33	0.09	−2.11	−1.96	−2.04	0.15

Table S4. Electrochemical data of [U^{VI}O_2(L2)DMSO] in DMSO containing 0.1 M *tetra-n-*butylammonium perchlorate at 295 K. Potentials show the relative values to that of the Fc^{0/+} redox couple.

Scan rate	$E_{pc,1}$ / V	$E_{pa,1}$ / V	E_1°' / V	$\Delta E_{p,1}$ / V	$E_{pc,2}$ / V	$E_{pa,2}$ / V	E_2°' / V	$\Delta E_{p,2}$ / V
50 mV·s⁻¹	−0.82	−0.75	−0.79	0.07	−1.44	−1.36	−1.40	0.08
100 mV·s⁻¹	−0.82	−0.75	−0.79	0.07	−1.45	−1.36	−1.41	0.09
200 mV·s⁻¹	−0.82	−0.75	−0.79	0.07	−1.45	−1.36	−1.41	0.09
500 mV·s⁻¹	−0.83	−0.74	−0.79	0.09	−1.46	−1.35	−1.41	0.11

Table S5. Electrochemical data of [U^{VI}O_2(L3)] in DMSO containing 0.1 M *tetra-n-*butylammonium perchlorate at 295 K. Potentials show the relative values to that of the Fc^{0/+} redox couple.

Scan rate	$E_{pc,1}$ / V	$E_{pa,1}$ / V	E_1°' / V	$\Delta E_{p,1}$ / V	$E_{pc,2}$ / V	$E_{pa,2}$ / V	E_2°' / V	$\Delta E_{p,2}$ / V
50 mV·s⁻¹	−1.40	−1.33	−1.37	0.07	−2.03	−1.95	−1.99	0.08
100 mV·s⁻¹	−1.40	−1.33	−1.37	0.07	−2.03	−1.95	−1.99	0.08
200 mV·s⁻¹	−1.41	−1.33	−1.37	0.08	−2.03	−1.95	−1.99	0.08
500 mV·s⁻¹	−1.41	−1.33	−1.37	0.08	−2.03	−1.95	−1.99	0.08

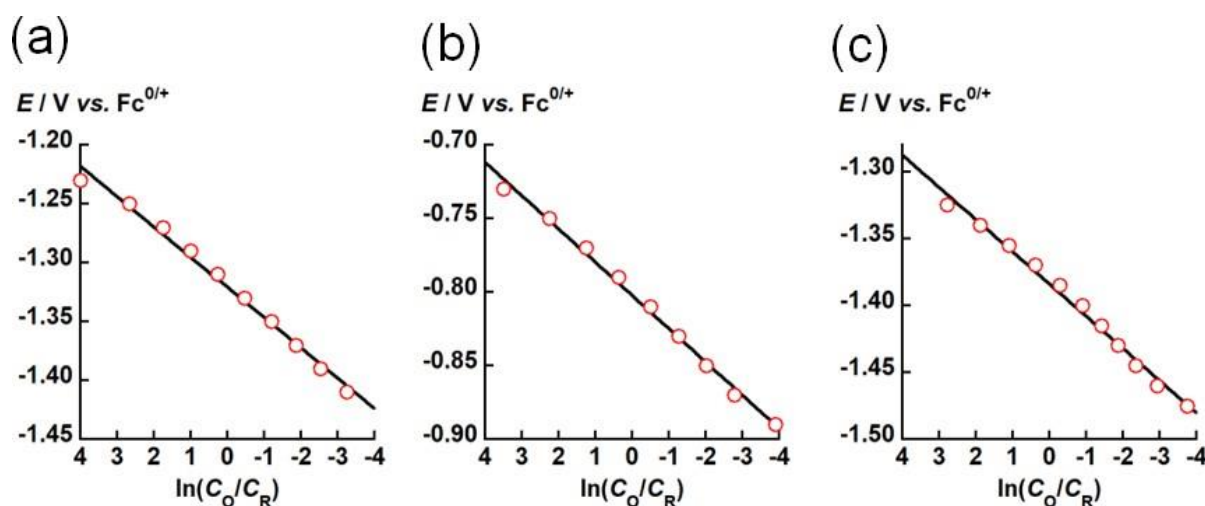**Figure S11.** Nernstian plot for the spectral change of the electrochemical reduction of $[U^{VI}O_2(Lx)DMSO_y]$ (x = 1-3, y = 0-1). $[U^{VI}O_2(L1)DMSO]$ (a), $[U^{VI}O_2(L2)DMSO]$ (b), and $[U^{VI}O_2(L3)]$ (c). The C_O/C_R was calculated from the absorbance at 19157 cm^{-1} (a), 22989 cm^{-1} (b) and 21322 cm^{-1} (c).
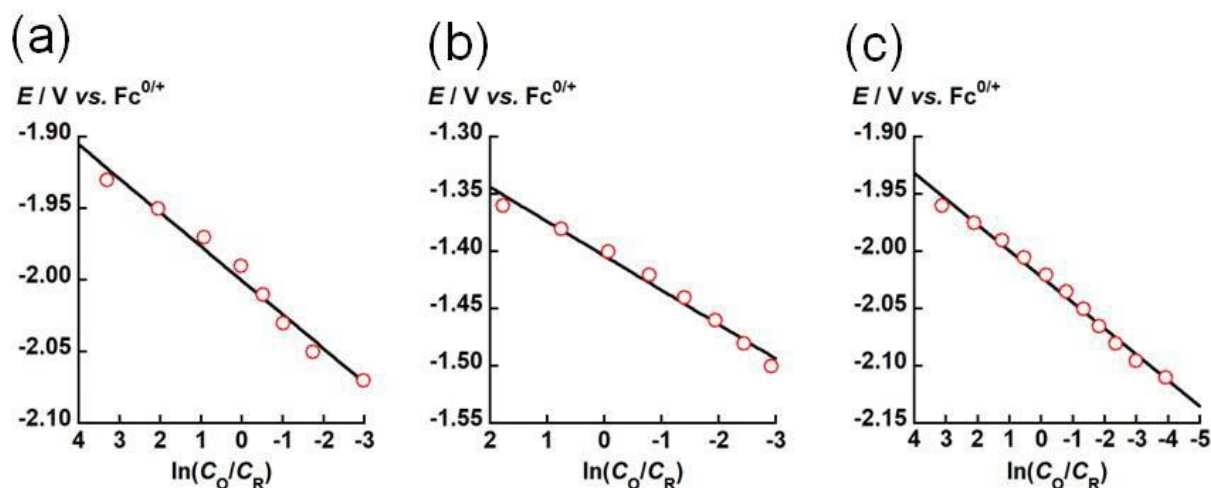

Figure S12. Nernstian plot for the spectral change of the electrochemical reduction of $[UO_2(Lx)(DMSO)_y]^-$ (x = 1-3, y = 0-1). $[UO_2(L1)DMSO]^-$ (a), $[UO_2(L2)DMSO]^-$ (b), and $[UO_2(L3)]^-$ (c). The C_O/C_R was calculated from the absorbance at 19157 cm^{-1} (a), 25000 cm^{-1} (b) and 19685 cm^{-1} (c).
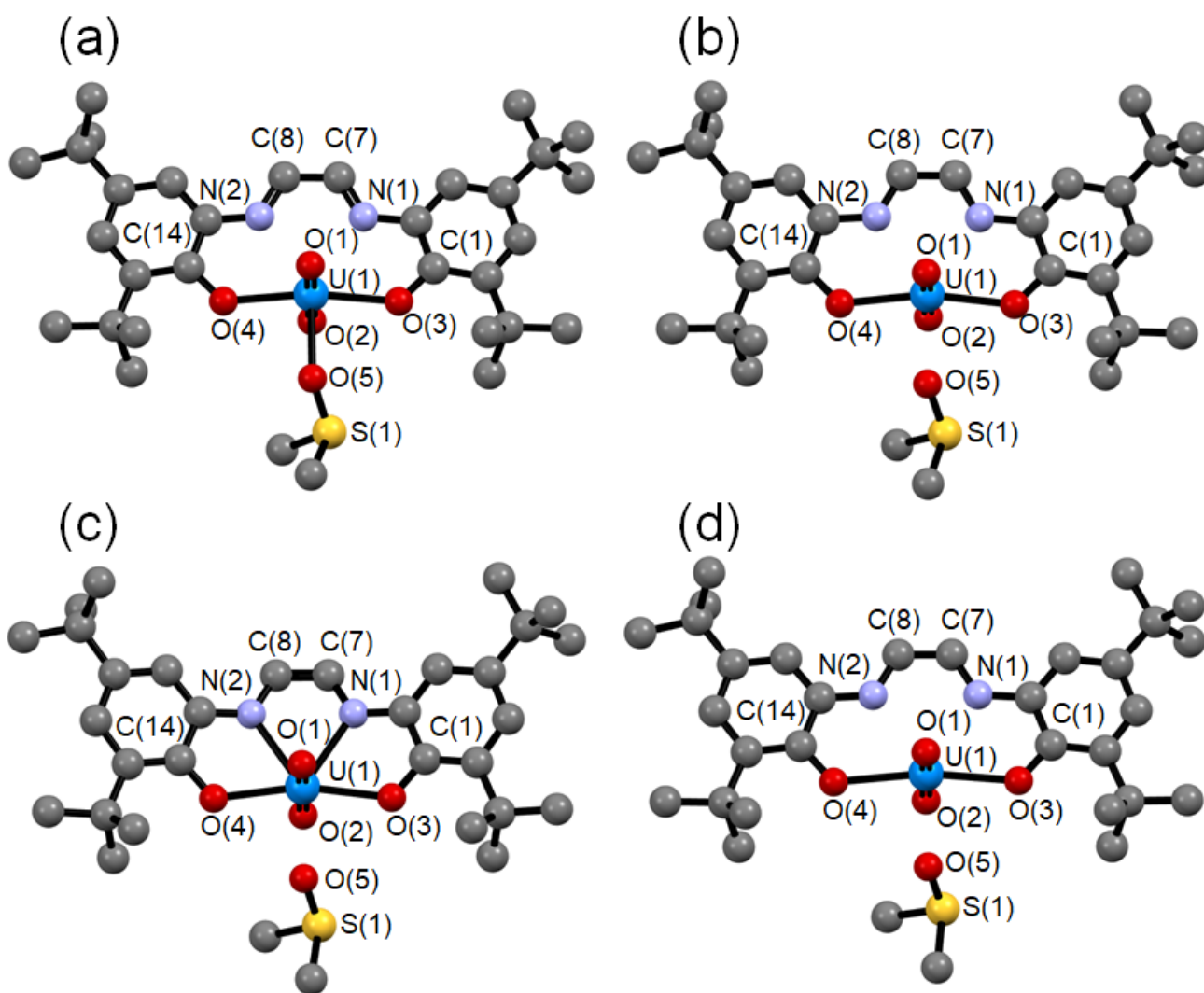
Figure S13. The optimized structures of $[U^{VI}O_2(L1)DMSO]$ (a), $[UO_2(L1)DMSO]^-$ (b), $[UO_2(L1)DMSO]^{2-}$ ($S_T = 0$) (c), and $[UO_2(L1)DMSO]^{2-}$ ($S_T = 1$) (d). Hydrogen atoms are omitted for clarity.

Table S6. The selected bond lengths of calculated structures of $[U^{VI}O_2(L1)DMSO]$, $[UO_2(L1)DMSO]^-$, $[UO_2(L1)DMSO]^{2-}$ ($S_T = 0$), and $[UO_2(L1)DMSO]^{2-}$ ($S_T = 1$) (Å).

	$[U^{VI}O_2(L1)DMSO]$	$[UO_2(L1)DMSO]^-$	$[UO_2(L1)DMSO]^{2-}$ ($S_T = 0$)	$[UO_2(L1)DMSO]^{2-}$ ($S_T = 1$)
U(1)−O(1)	1.795	1.809	1.831	1.873
U(1)−O(2)	1.798	1.813	1.838	1.882
U(1)−O(3)	2.309	2.308	2.355	2.432
U(1)−O(4)	2.299	2.303	2.353	2.431
U(1)−O(5)	2.393	2.448	2.524	2.546
U(1)−N(1)	2.602	2.536	2.448	2.595
U(1)−N(2)	2.599	2.534	2.449	2.593
C(7)−N(1)	1.300	1.341	1.383	1.339
C(8)−N(2)	1.299	1.341	1.365	1.339
C(7)−C(8)	1.437	1.394	1.365	1.400
C(1)−O(3)	1.311	1.328	1.335	1.312
C(14)−O(4)	1.315	1.329	1.335	1.313
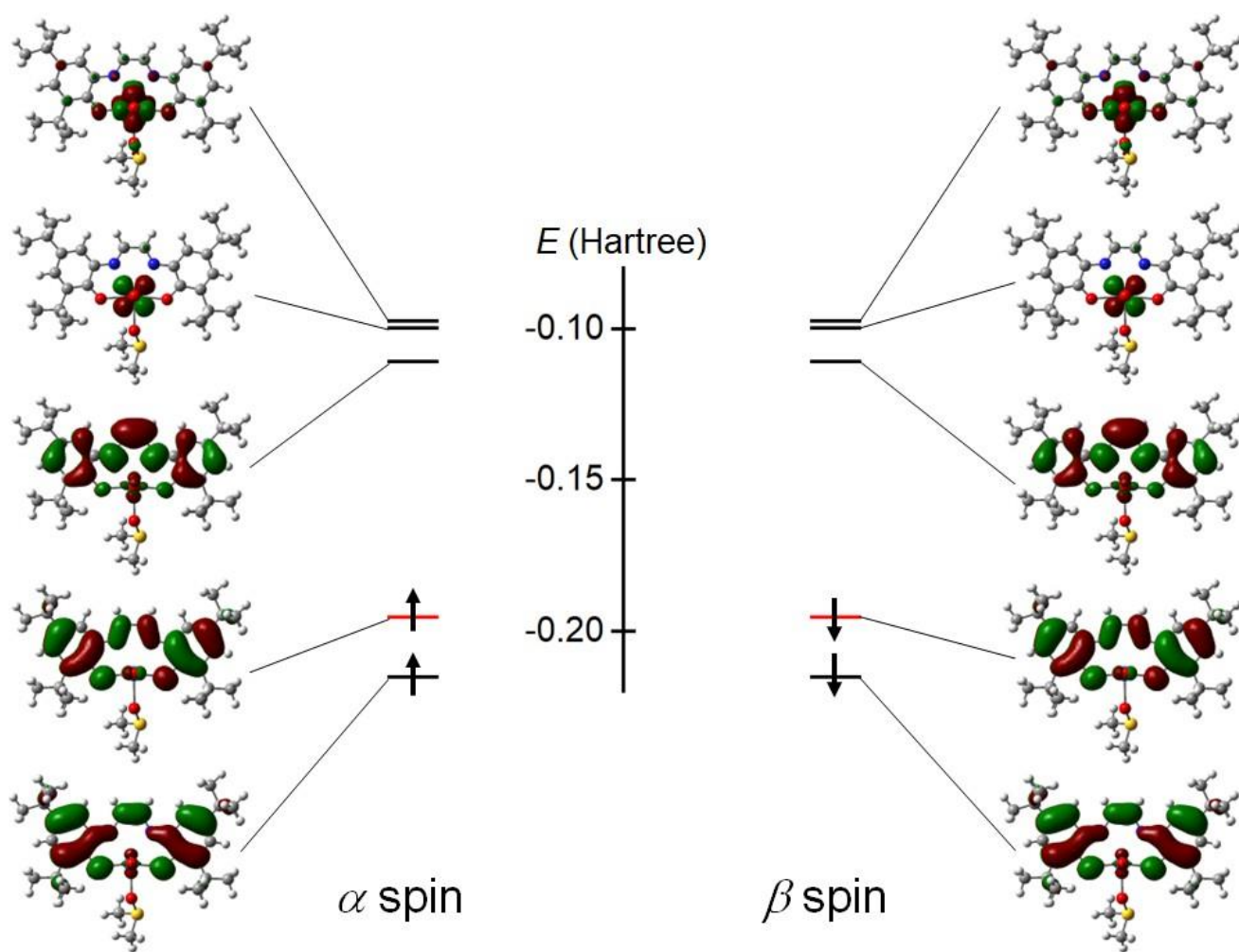
Figure S14. Calculated MO energy diagrams of [U^{VI}O$_2$(L1)DMSO].
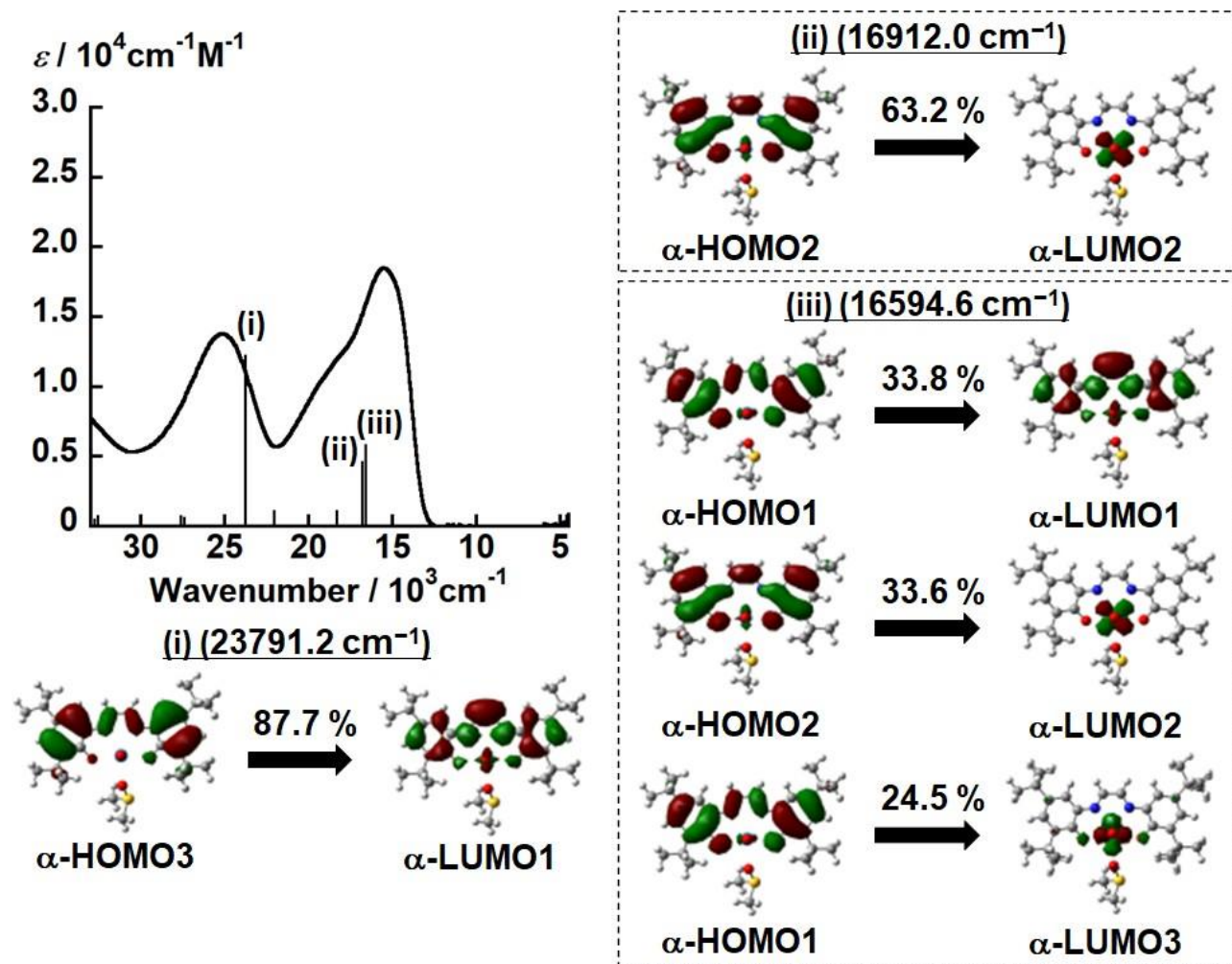
Figure S15. UV-vis-NIR spectrum of [U^{VI}O$_2$(L1)DMSO] in DMSO and predicted band positions and intensities of the TD-DFT calculation. The vertical black lines correspond to the calculated transitions for [U^{VI}O$_2$(L1)DMSO].
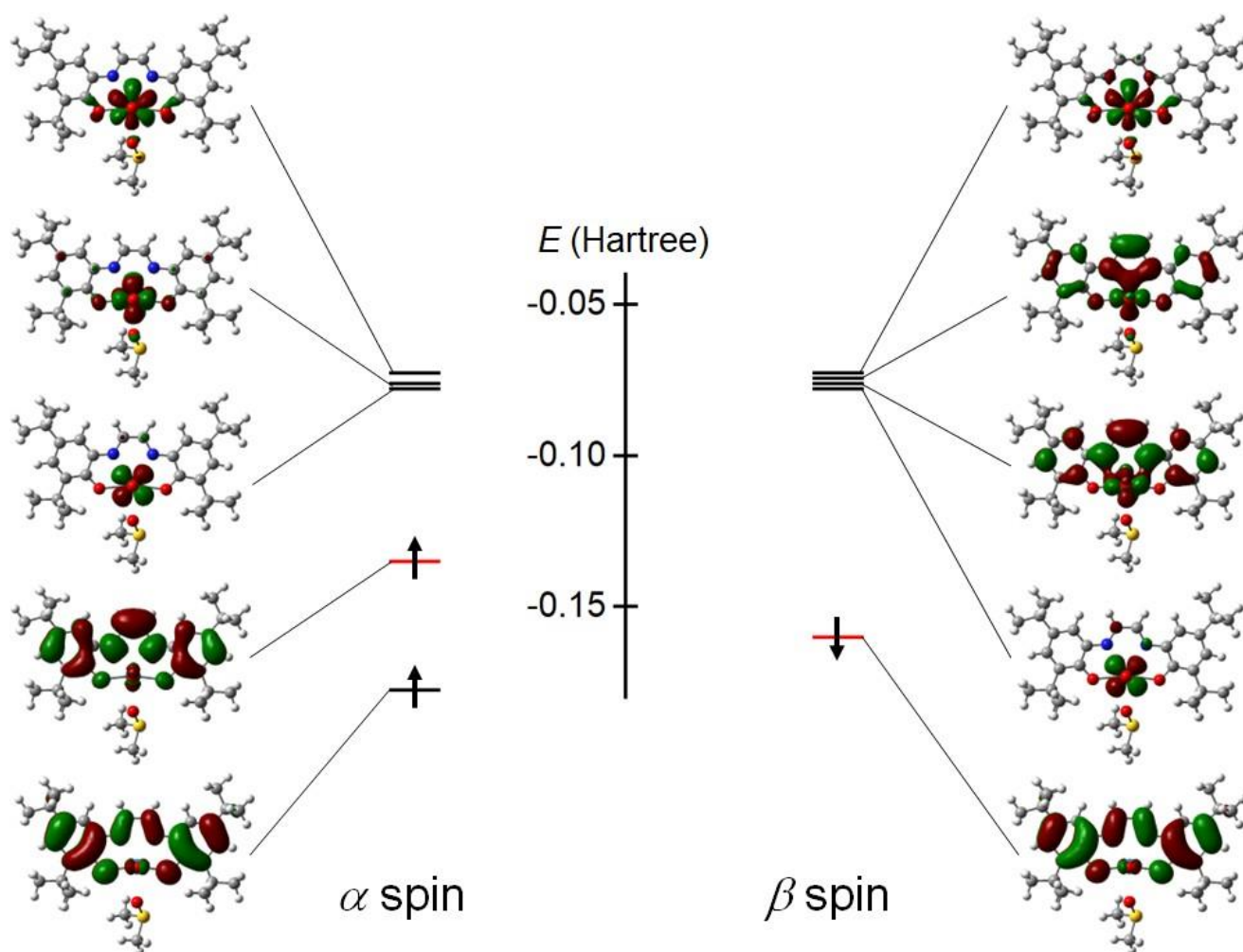
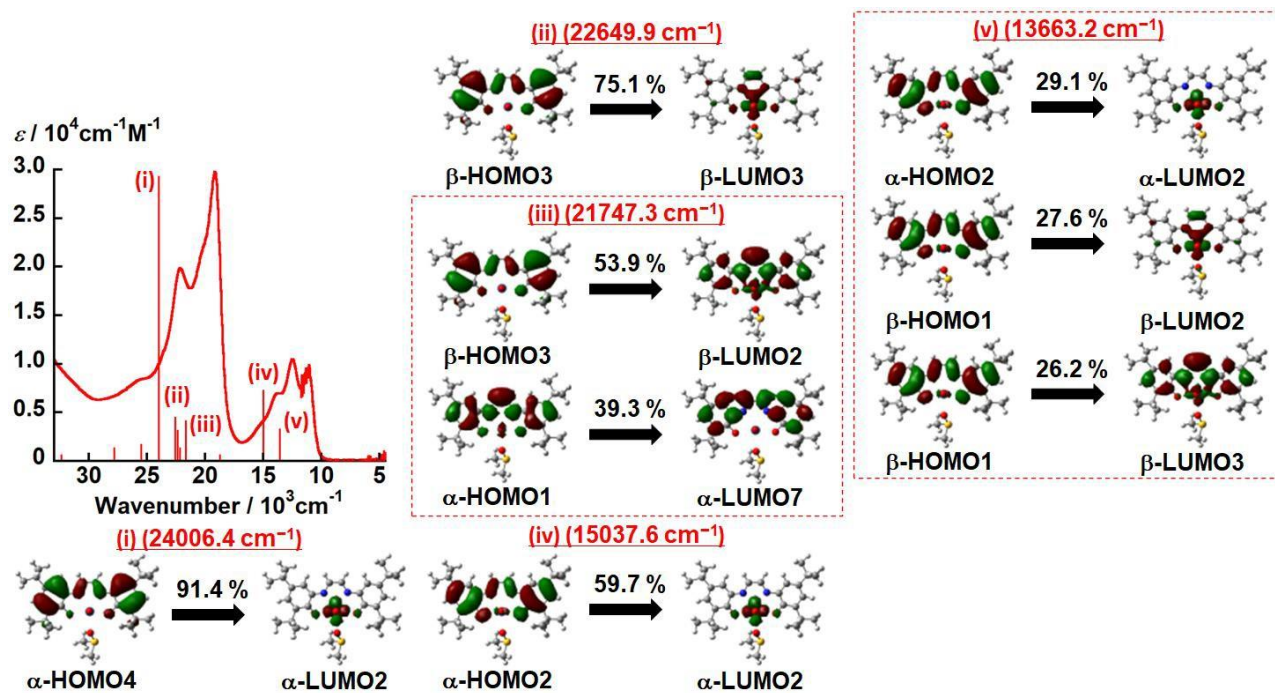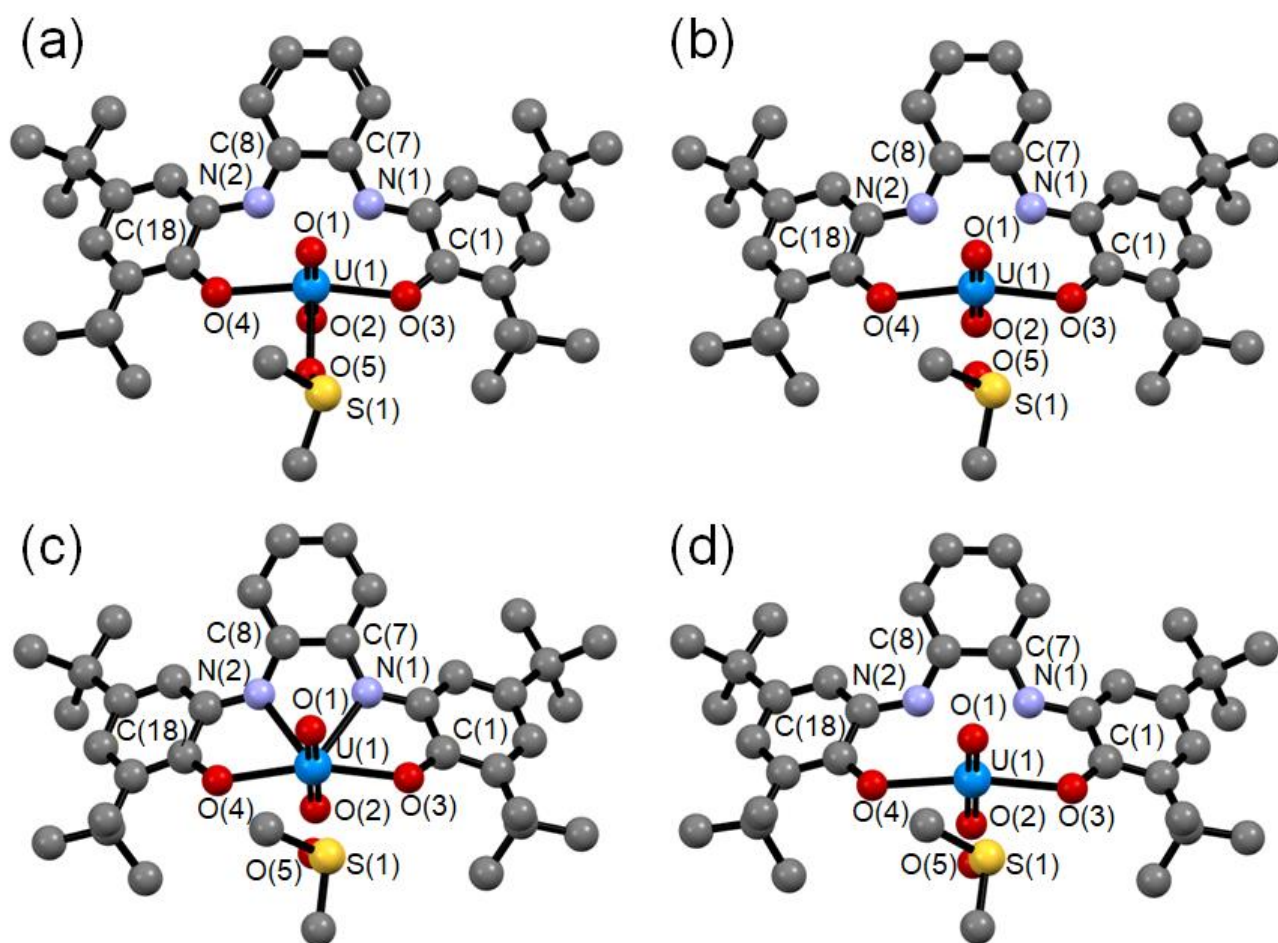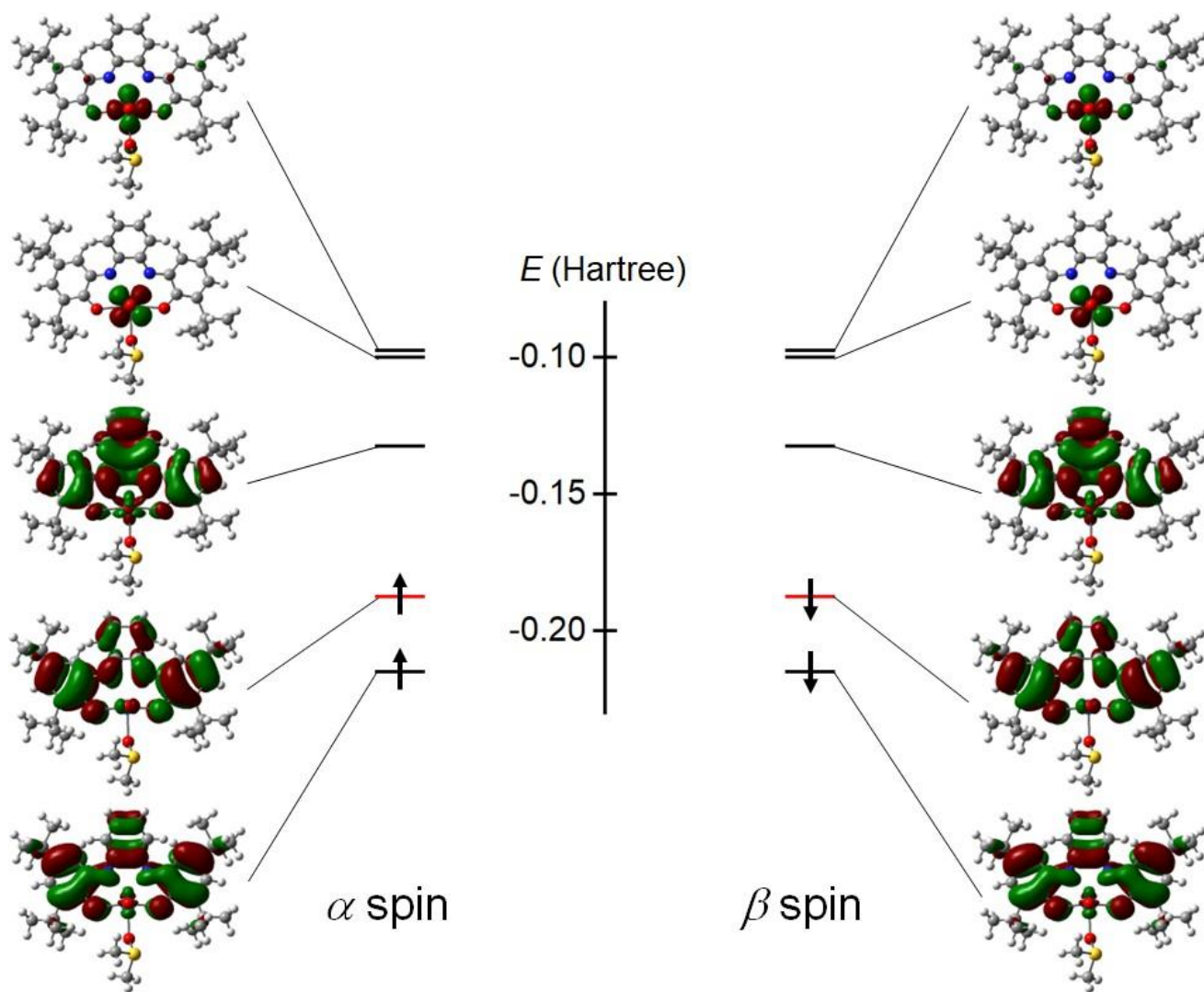**Figure S16.** Calculated MO energy diagrams of [UO$_2$(L1)DMSO]$^-$.

Figure S17. UV-vis-NIR spectrum of [UO$_2$(L1)DMSO]$^-$ in DMSO and predicted band positions and intensities of the TD-DFT calculation. The vertical red lines correspond to the calculated transitions for [UO$_2$(L1)DMSO]$^-$.

Figure S18. The optimized structures of [U^{VI}O$_2$(L2)DMSO] (a), [UO$_2$(L2)DMSO]$^-$ (b), [UO$_2$(L2)DMSO]$^{2-}$ (S_T = 0) (c), and [UO$_2$(L2)DMSO]$^{2-}$ (S_T = 1) (d). Hydrogen atoms are omitted for clarity.

Table S7. The selected bond lengths of calculated structures of [U^{VI}O$_2$(L2)DMSO], [UO$_2$(L2)DMSO]$^-$, [UO$_2$(L2)DMSO]$^{2-}$ (S_T = 0), and [UO$_2$(L2)DMSO]$^{2-}$ (S_T = 1) (Å).

	[UO$_2$(L2)DMSO]	[UO$_2$(L2)DMSO]$^-$	[UO$_2$(L2)DMSO]$^{2-}$ (S_T = 0)	[UO$_2$(L2)DMSO]$^{2-}$ (S_T = 1)
U(1)−O(1)	1.799	1.814	1.836	1.881
U(1)−O(2)	1.795	1.809	1.828	1.871
U(1)−O(3)	2.306	2.314	2.343	2.427
U(1)−O(4)	2.306	2.312	2.341	2.427
U(1)−O(5)	2.393	2.451	2.523	2.545
U(1)−N(1)	2.585	2.514	2.436	2.584
U(1)−N(2)	2.578	2.511	2.436	2.584
C(7)−N(1)	1.327	1.355	1.384	1.351
C(8)−N(2)	1.326	1.354	1.384	1.351
C(7)−C(8)	1.480	1.461	1.447	1.470
C(1)−O(3)	1.310	1.325	1.334	1.311
C(18)−O(4)	1.312	1.326	1.334	1.311

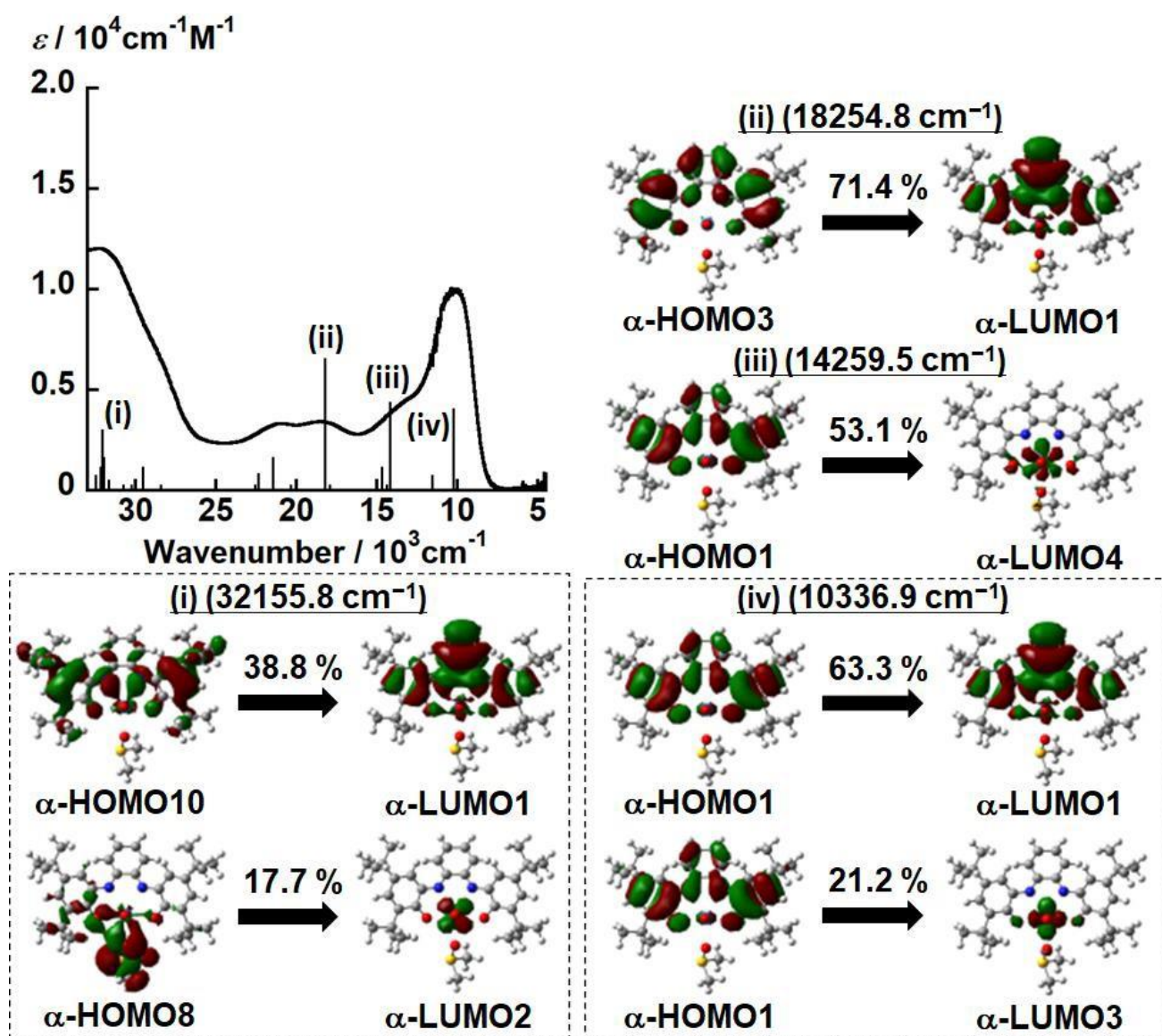**Figure S19.** Calculated MO energy diagrams of [$U^{VI}O_2$(L2)DMSO].

Figure S20. UV-vis-NIR spectrum of [$U^{VI}O_2$(L2)DMSO] in DMSO and predicted band positions and intensities of the TD-DFT calculation. The vertical black lines correspond to the calculated transitions for [$U^{VI}O_2$(L2)DMSO].
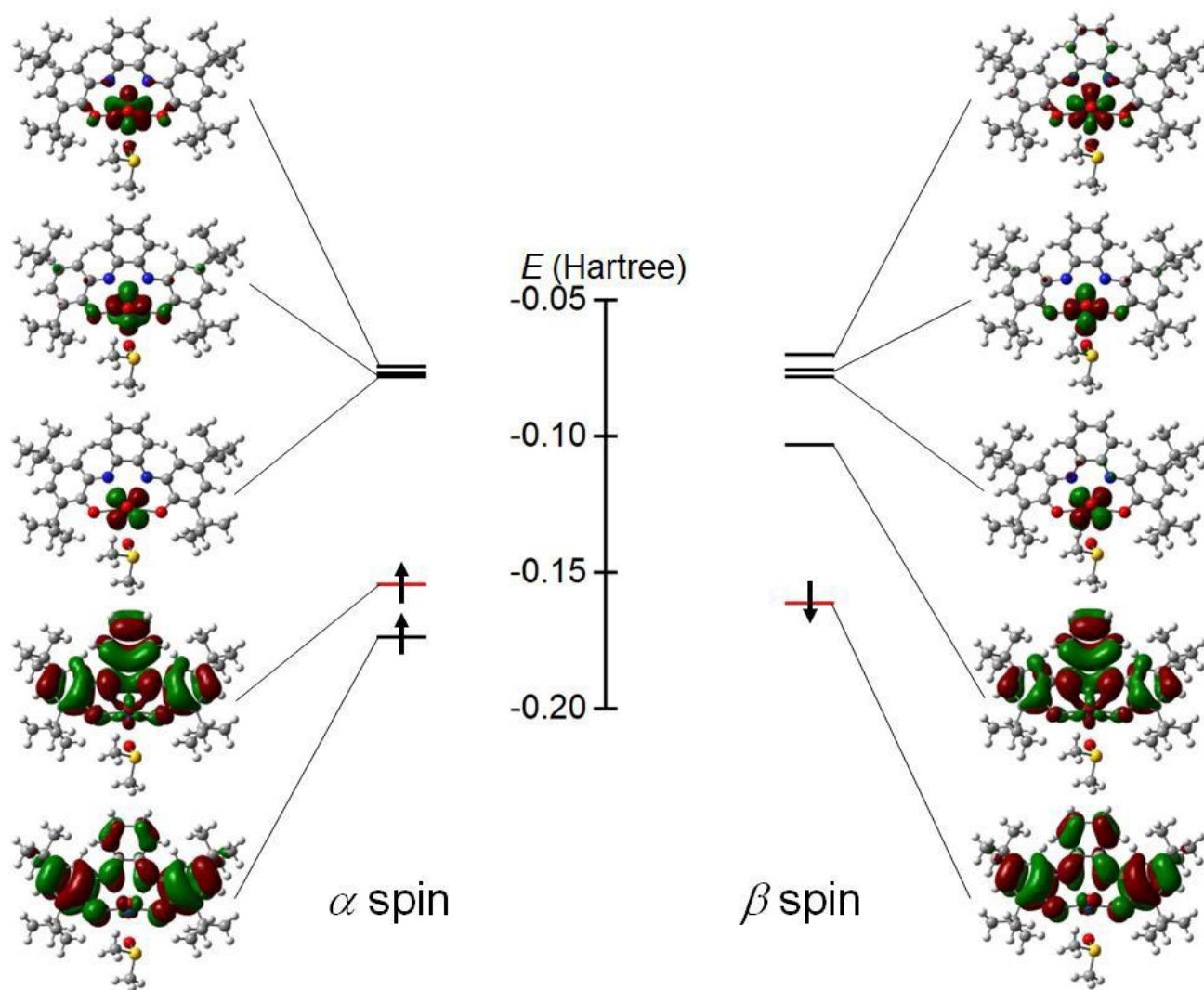
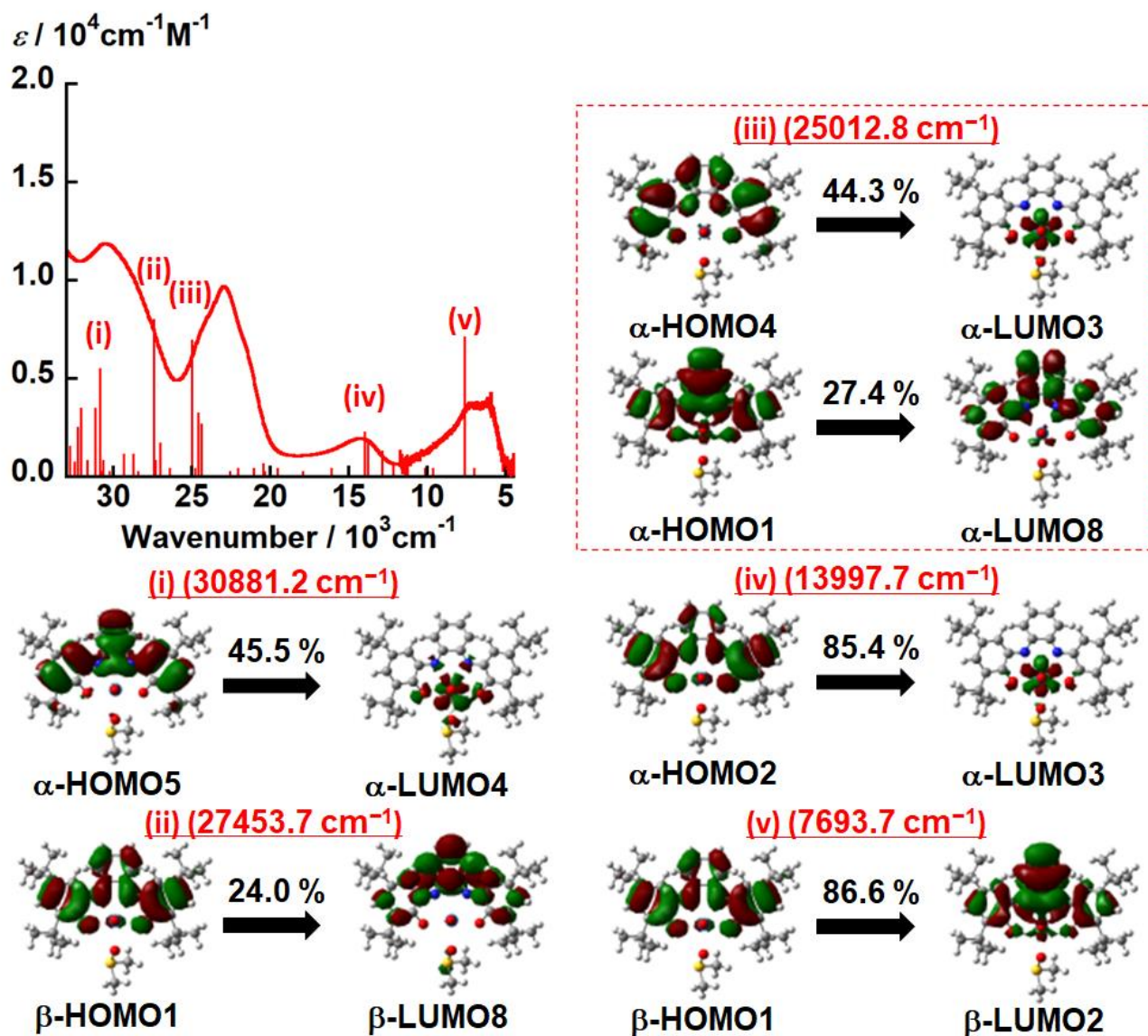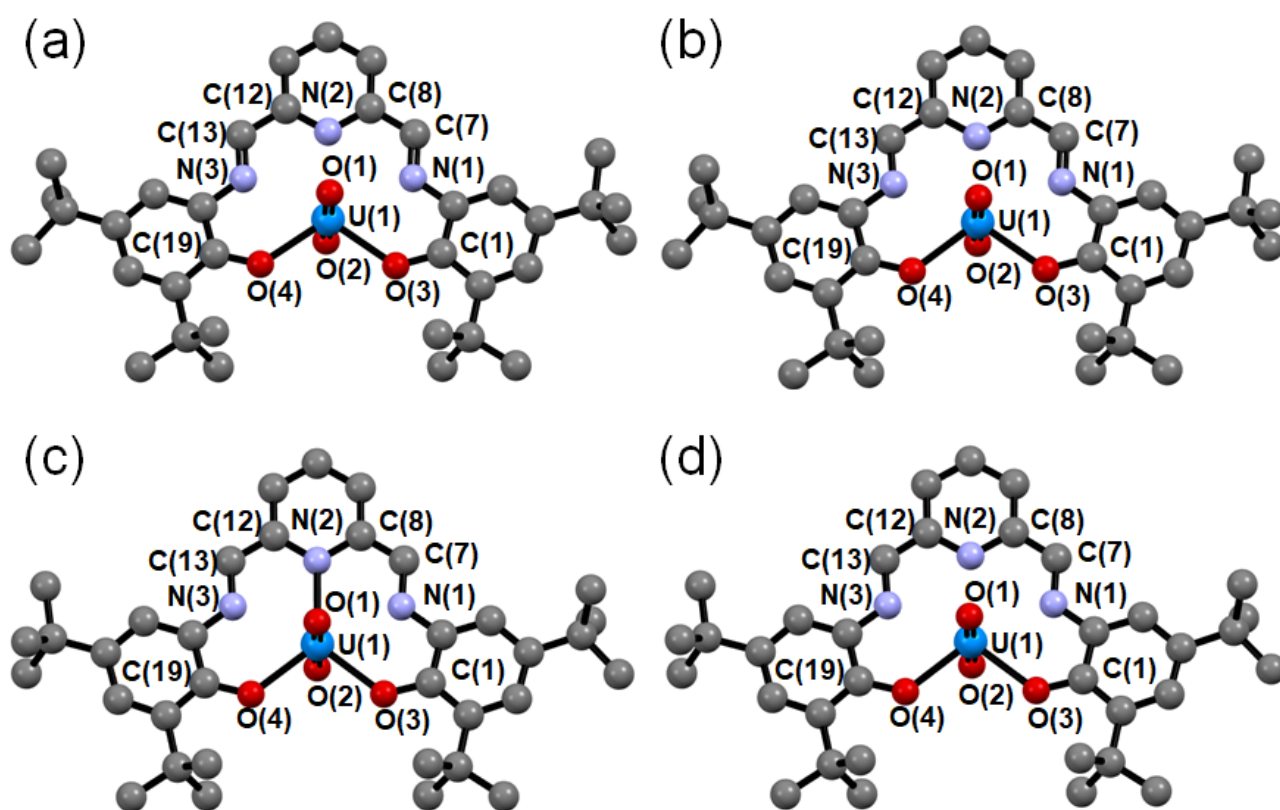**Figure S21.** Calculated MO energy diagrams of [UO$_2$(L2)DMSO]$^-$.

Figure S22. UV-vis-NIR spectrum of $[UO_2(L2)DMSO]^-$ in DMSO and predicted band positions and intensities of the TD-DFT calculation. The vertical red lines correspond to the calculated transitions for $[UO_2(L2)DMSO]^-$.

Figure S23. The optimized structures of [U^{VI}O$_2$(L3)] (a), [UO$_2$(L3)]$^-$ (b), [UO$_2$(L3)]$^{2-}$ (S_T = 0) (c), and [UO$_2$(L3)]$^{2-}$ (S_T = 1) (d). Hydrogen atoms are omitted for clarity.

Table S8. The selected bond lengths of calculated structures of $[U^{VI}O_2(L3)]$, $[UO_2(L3)]^-$, $[UO_2(L3)]^{2-}$ ($S_T = 0$), and $[UO_2(L3)]^{2-}$ ($S_T = 1$) (Å).

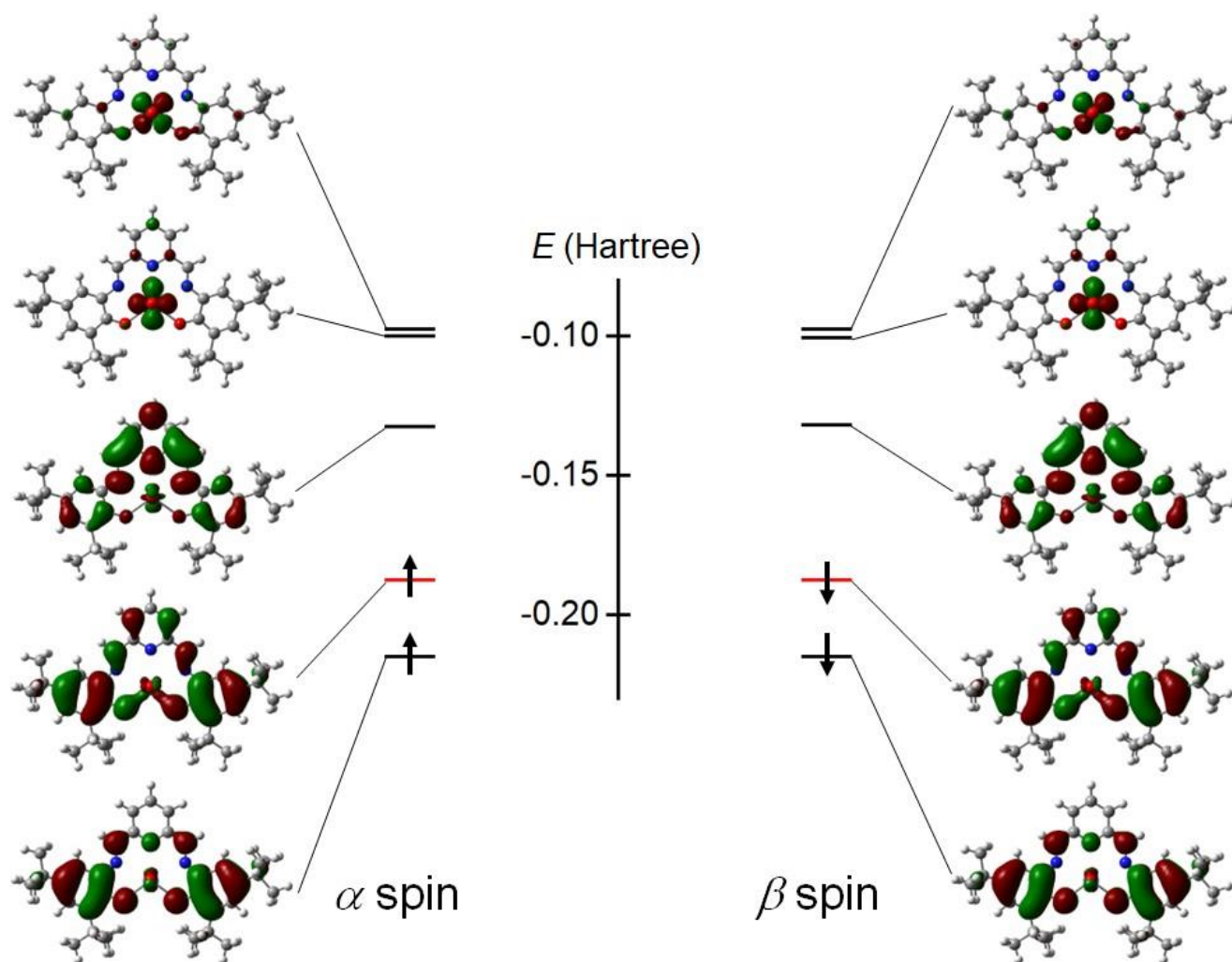|	$[U^{VI}O_2(L3)]$	$[UO_2(L3)]^-$	$[UO_2(L3)]^{2-}$ ($S_T = 0$)	$[UO_2(L3)]^{2-}$ ($S_T = 1$)
U(1)−O(1)	1.791	1.804	1.821	1.815
U(1)−O(2)	1.791	1.804	1.821	1.815
U(1)−O(3)	2.302	2.325	2.336	2.319
U(1)−O(4)	2.298	2.309	2.346	2.320
U(1)−N(1)	2.637	2.608	2.564	2.535
U(1)−N(2)	2.593	2.519	2.441	2.533
U(1)−N(3)	2.635	2.572	2.584	2.536
C(7)−N(1)	1.289	1.303	1.341	1.346
C(7)−C(8)	1.455	1.438	1.402	1.413
C(8)−N(2)	1.349	1.371	1.406	1.374
C(12)−N(2)	1.349	1.379	1.398	1.375
C(12)−C(13)	1.455	1.420	1.414	1.412
C(13)−N(3)	1.288	1.321	1.329	1.346
C(1)−O(3)	1.312	1.319	1.329	1.330
C(19)−O(4)	1.314	1.326	1.325	1.331

Figure S24. Calculated MO energy diagrams of [U^{VI}O$_2$(L3)].
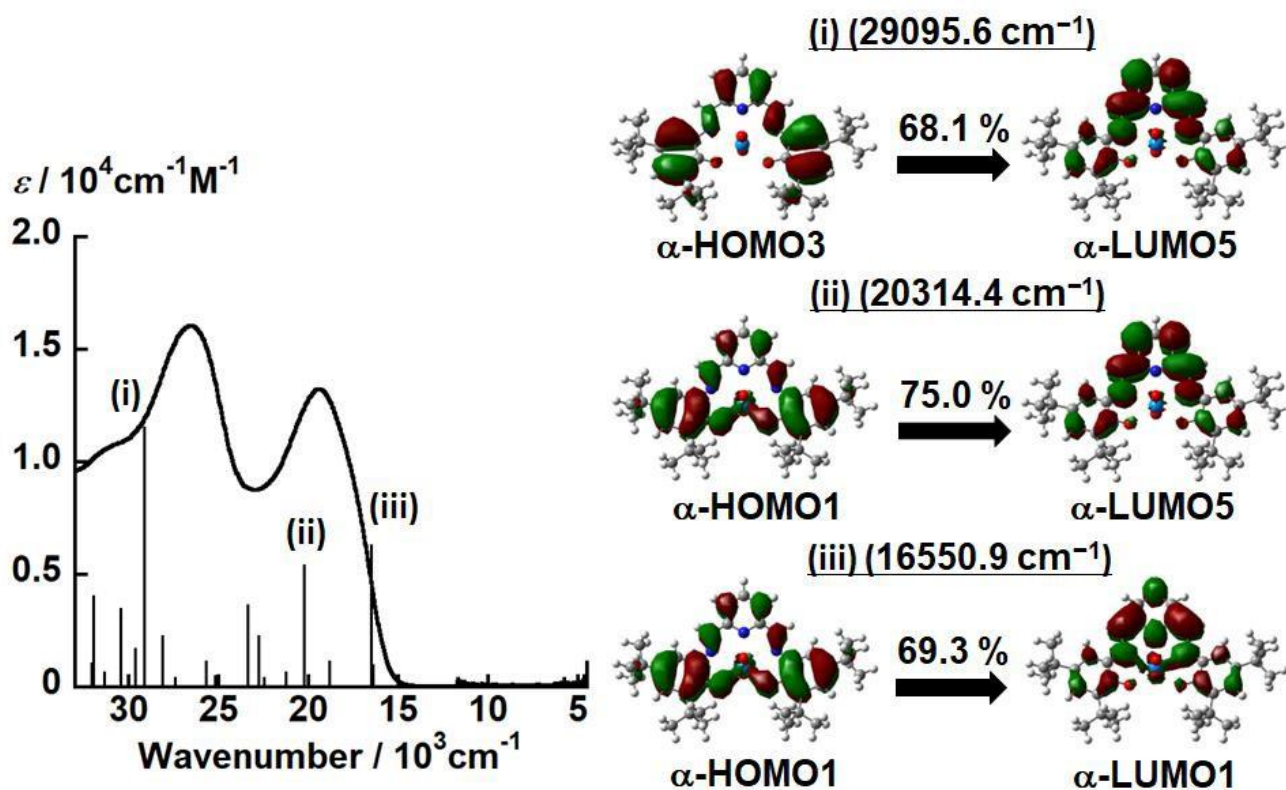
Figure S25. UV-vis-NIR spectrum of [U^{VI}O$_2$(L3)] in DMSO and predicted band positions and intensities of the TD-DFT calculation. The vertical black lines correspond to the calculated transitions for [U^{VI}O$_2$(L3)].
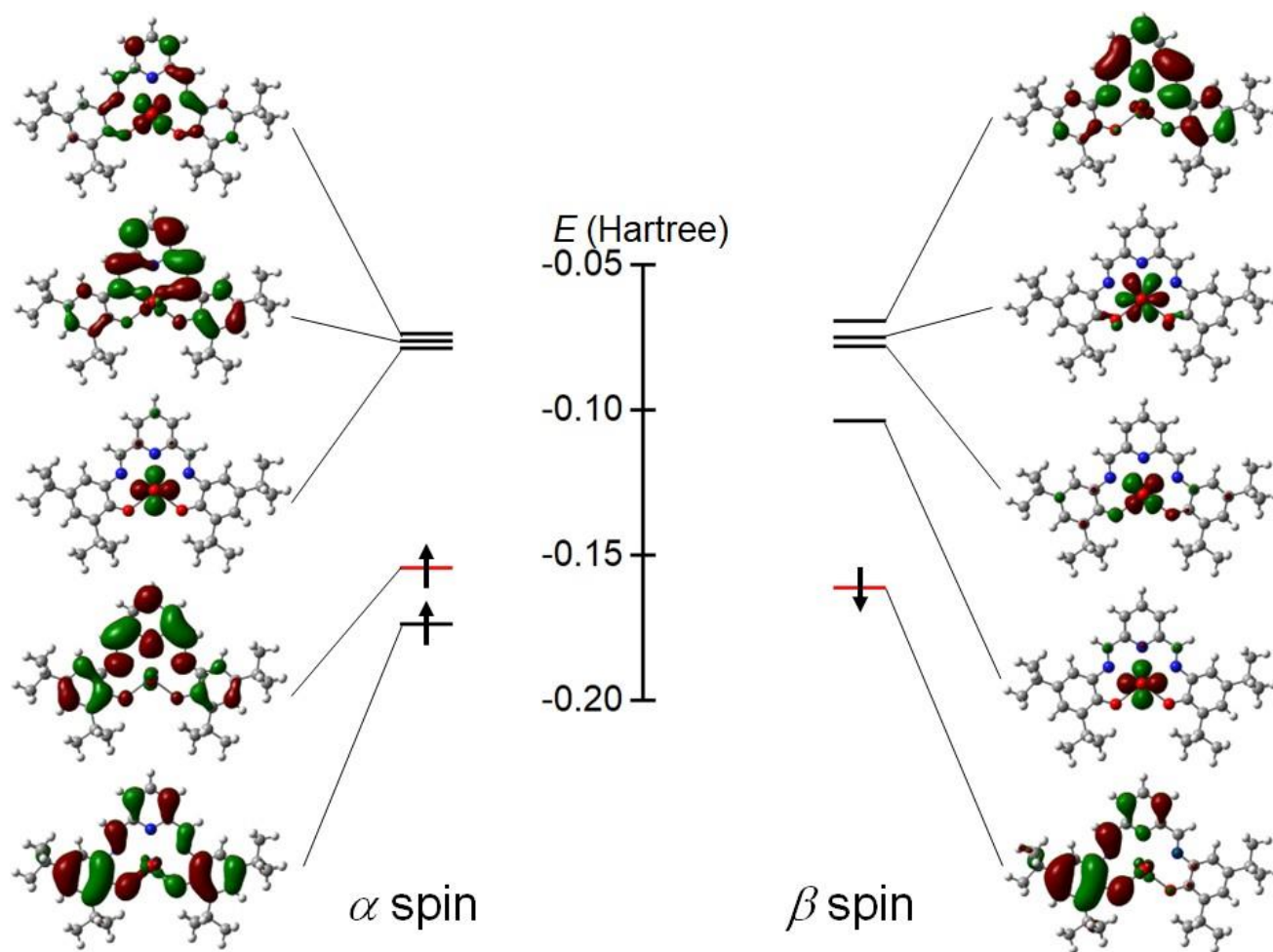
Figure S26. Calculated MO energy diagrams of [UO$_2$(L3)]$^-$.

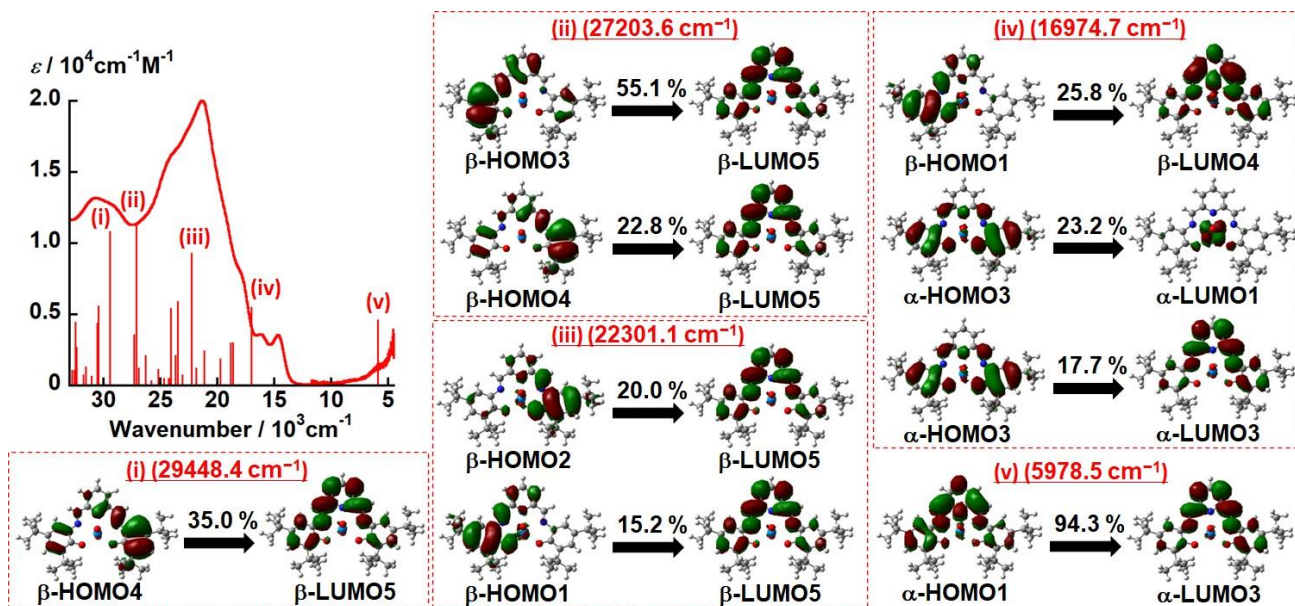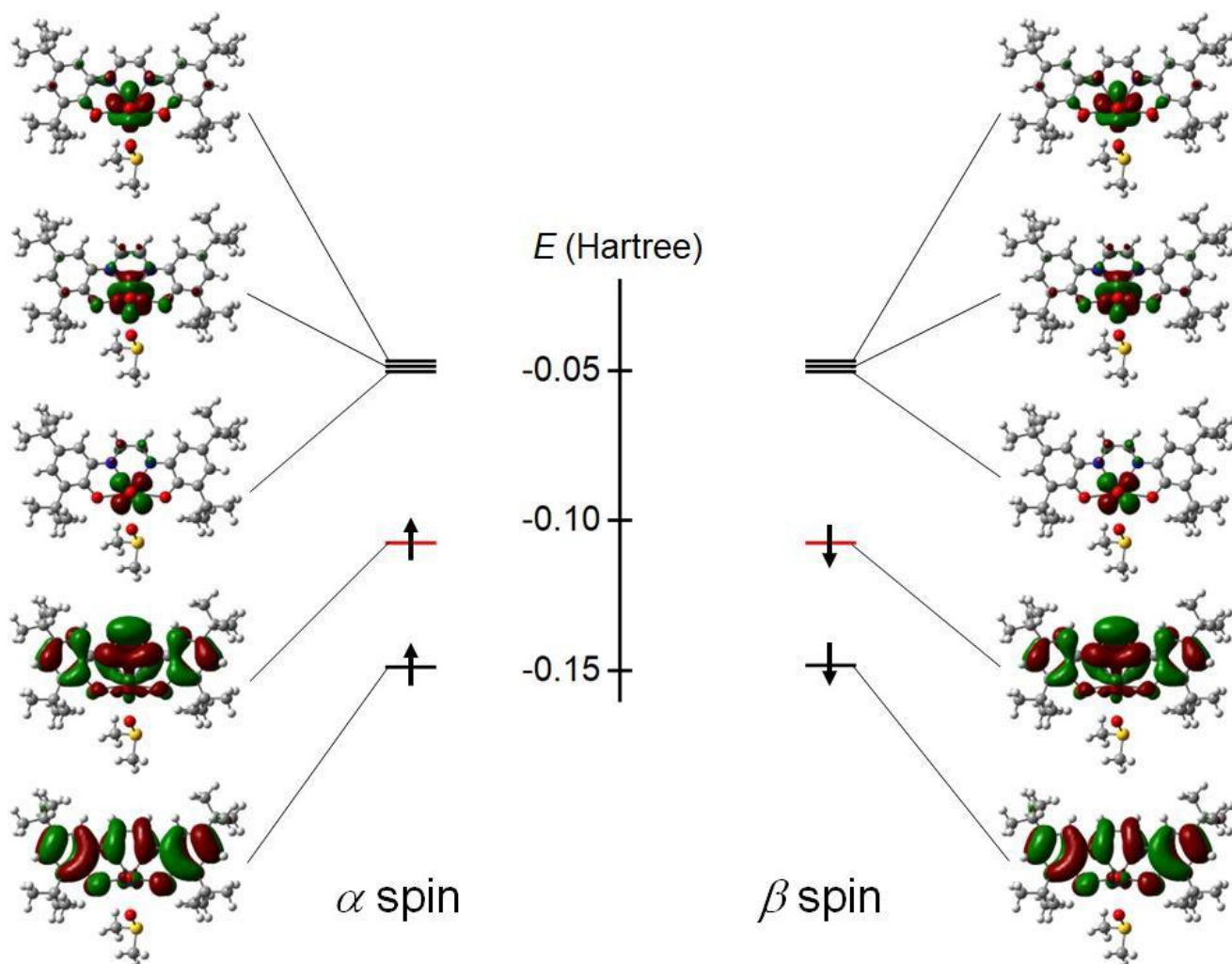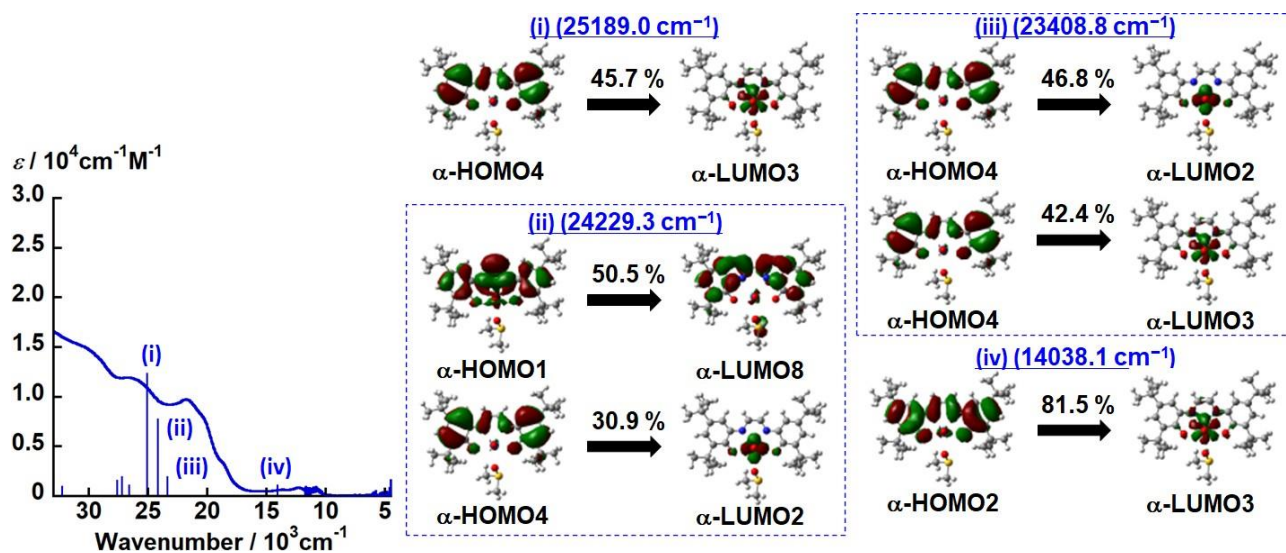**Figure S27.** UV-vis-NIR spectrum of $[UO_2(L3)]^-$ in DMSO and predicted band positions and intensities of the TD-DFT calculation. The vertical red lines correspond to the calculated transitions for $[UO_2(L3)]^-$.

Figure S28. Calculated MO energy diagrams of $[UO_2(L1)DMSO]^{2-}$ ($S_T = 0$).

Figure S29. UV-vis-NIR spectrum of $[UO_2(L1)DMSO]^{2-}$ in DMSO and predicted band positions and intensities of the TD-DFT calculation. The vertical blue lines correspond to the calculated transitions for $[UO_2(L1)DMSO]^{2-}$ with $S_T = 0$.
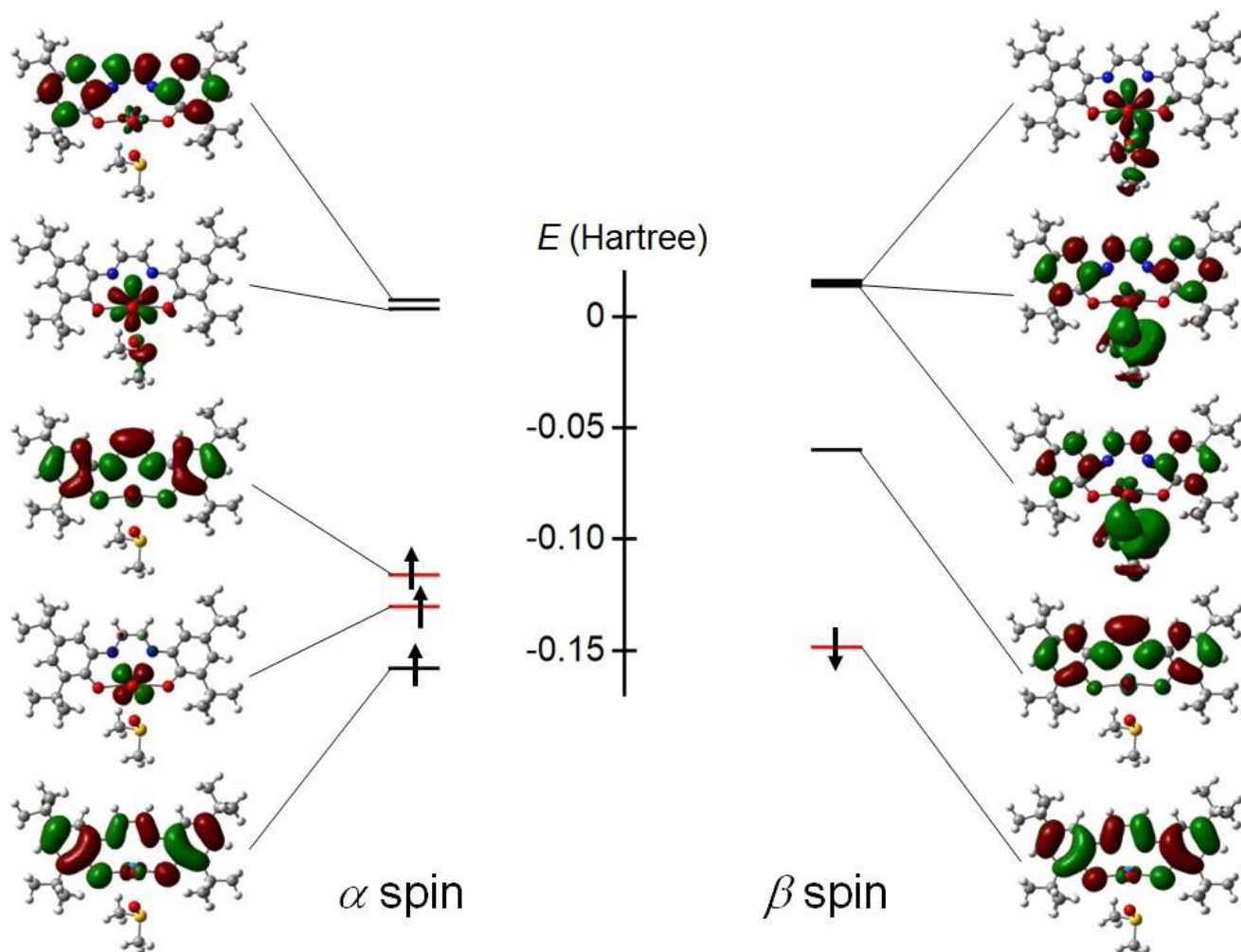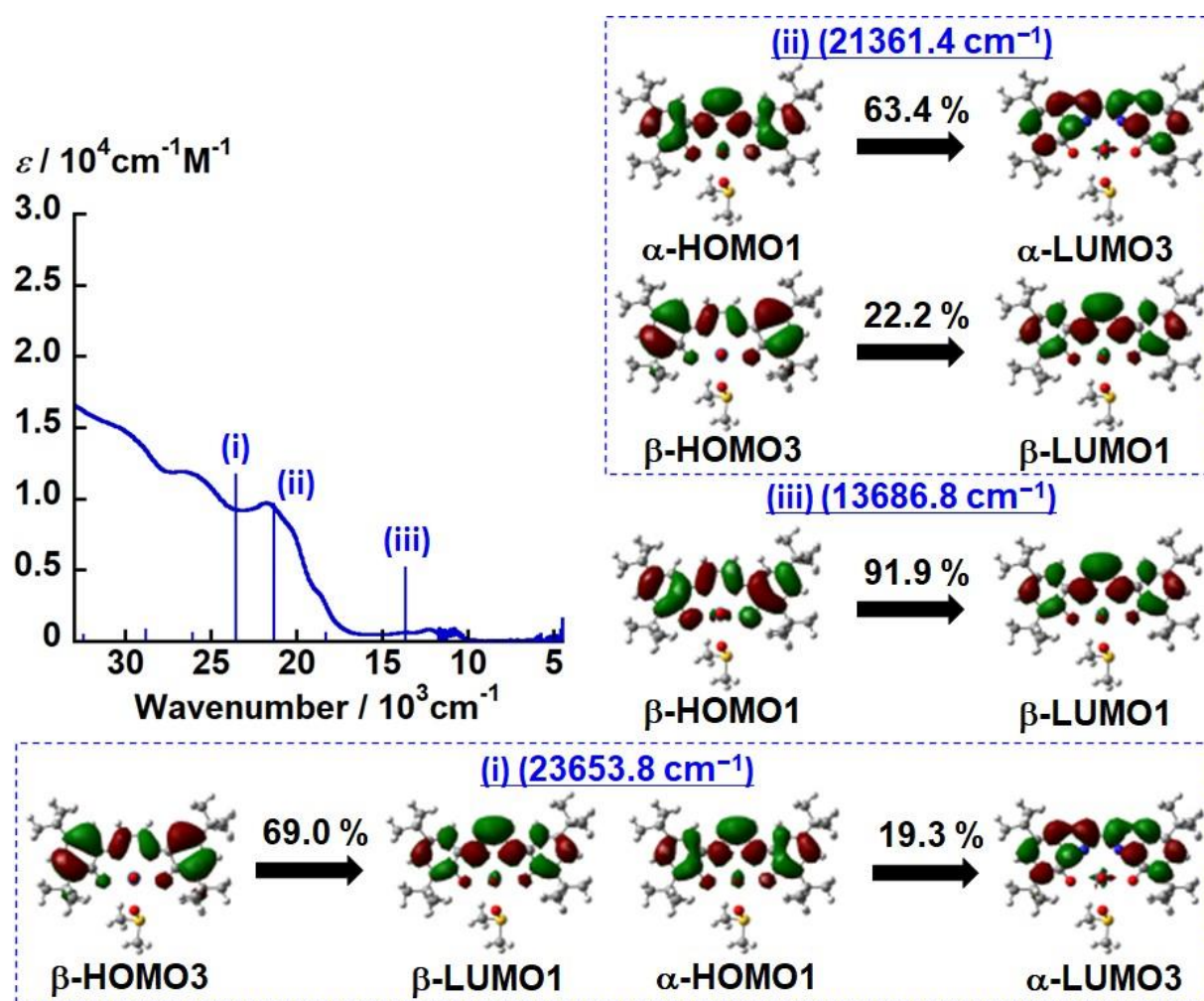
Figure S30. Calculated MO energy diagrams of $[UO_2(L1)DMSO]^{2-}$ ($S_T = 1$).

Figure S31. UV-vis-NIR spectrum of $[UO_2(L1)DMSO]^{2-}$ in DMSO and predicted band positions and intensities of the TD-DFT calculation. The vertical blue lines correspond to the calculated transitions for $[UO_2(L1)DMSO]^{2-}$ with $S_T = 1$.

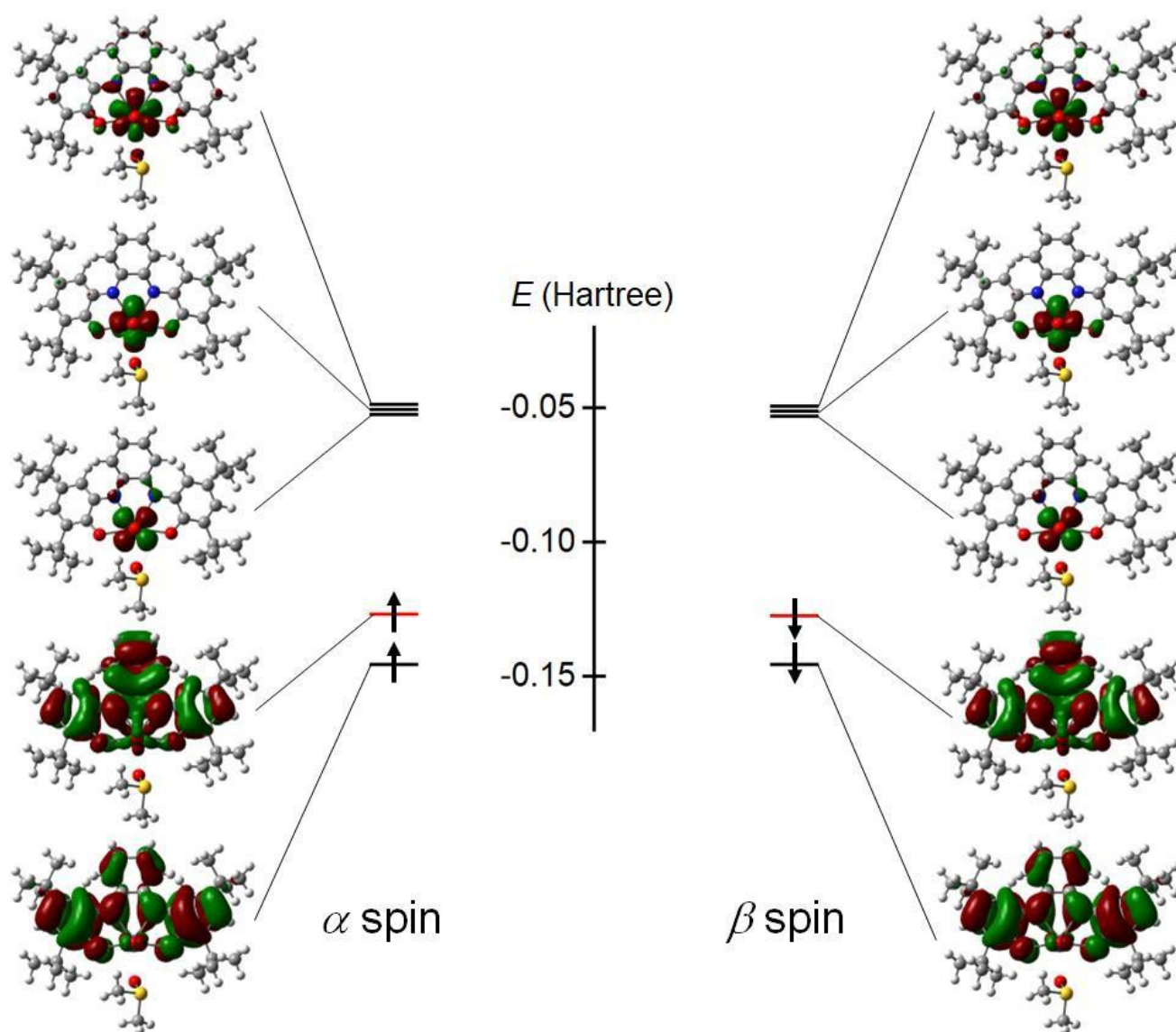**Figure S32.** Calculated MO energy diagrams of $[UO_2(L2)DMSO]^{2-}$ ($S_T = 0$).

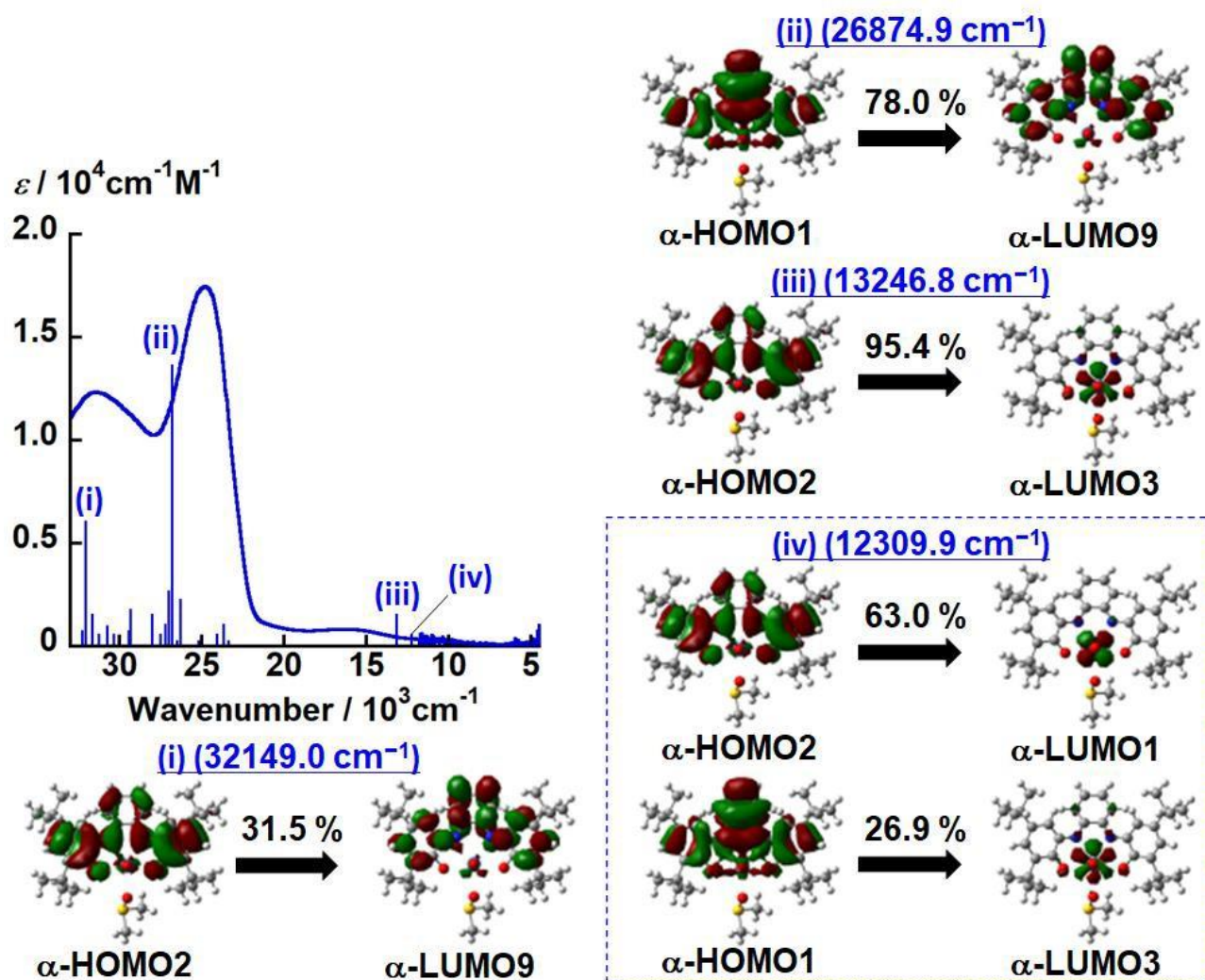**Figure S33.** UV-vis-NIR spectrum of [UO$_2$(L2)DMSO]$^{2-}$ in DMSO and predicted band positions and intensities of the TD-DFT calculation. The vertical blue lines correspond to the calculated transitions for [UO$_2$(L2)DMSO]$^{2-}$ with $S_T = 0$.

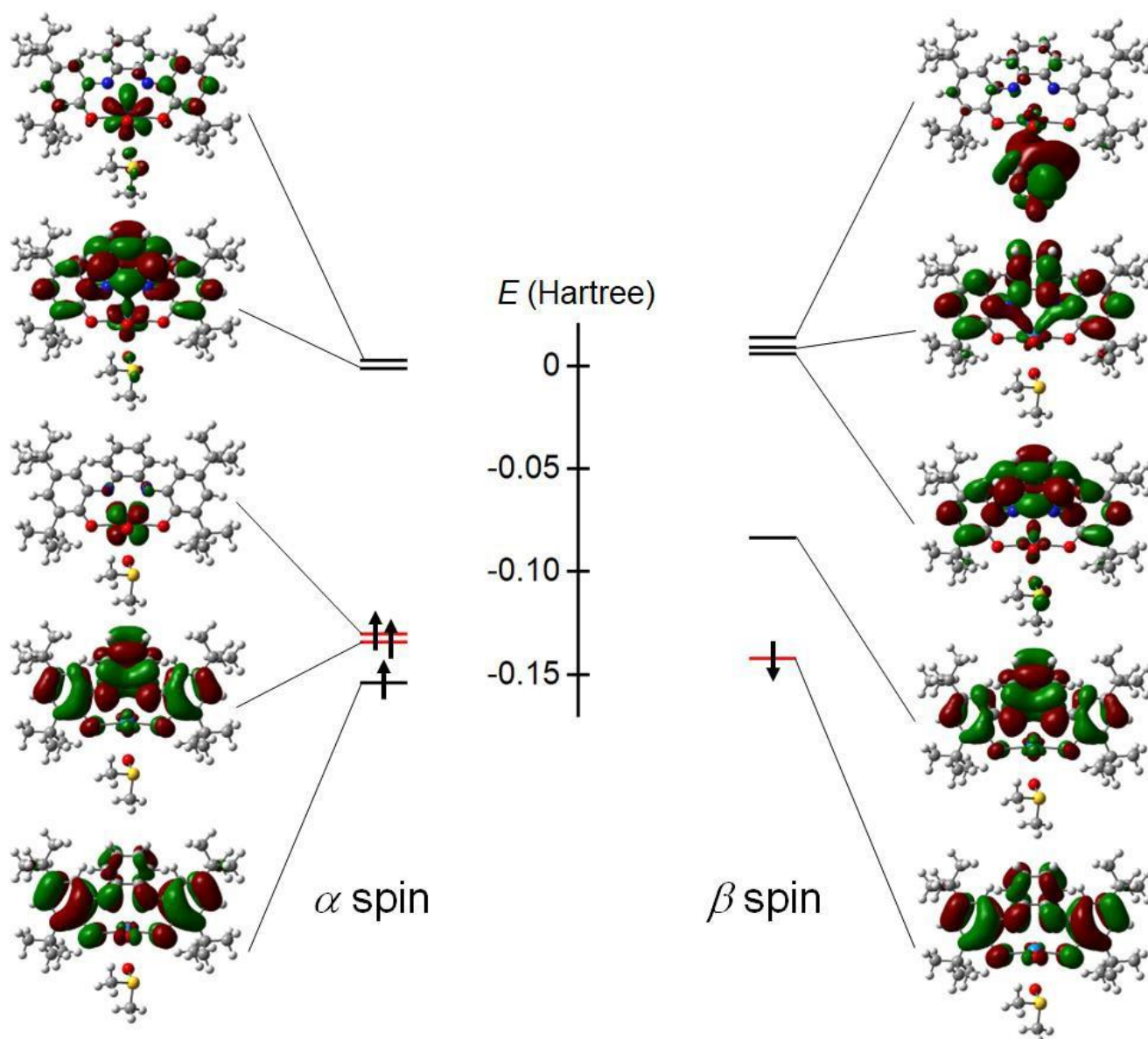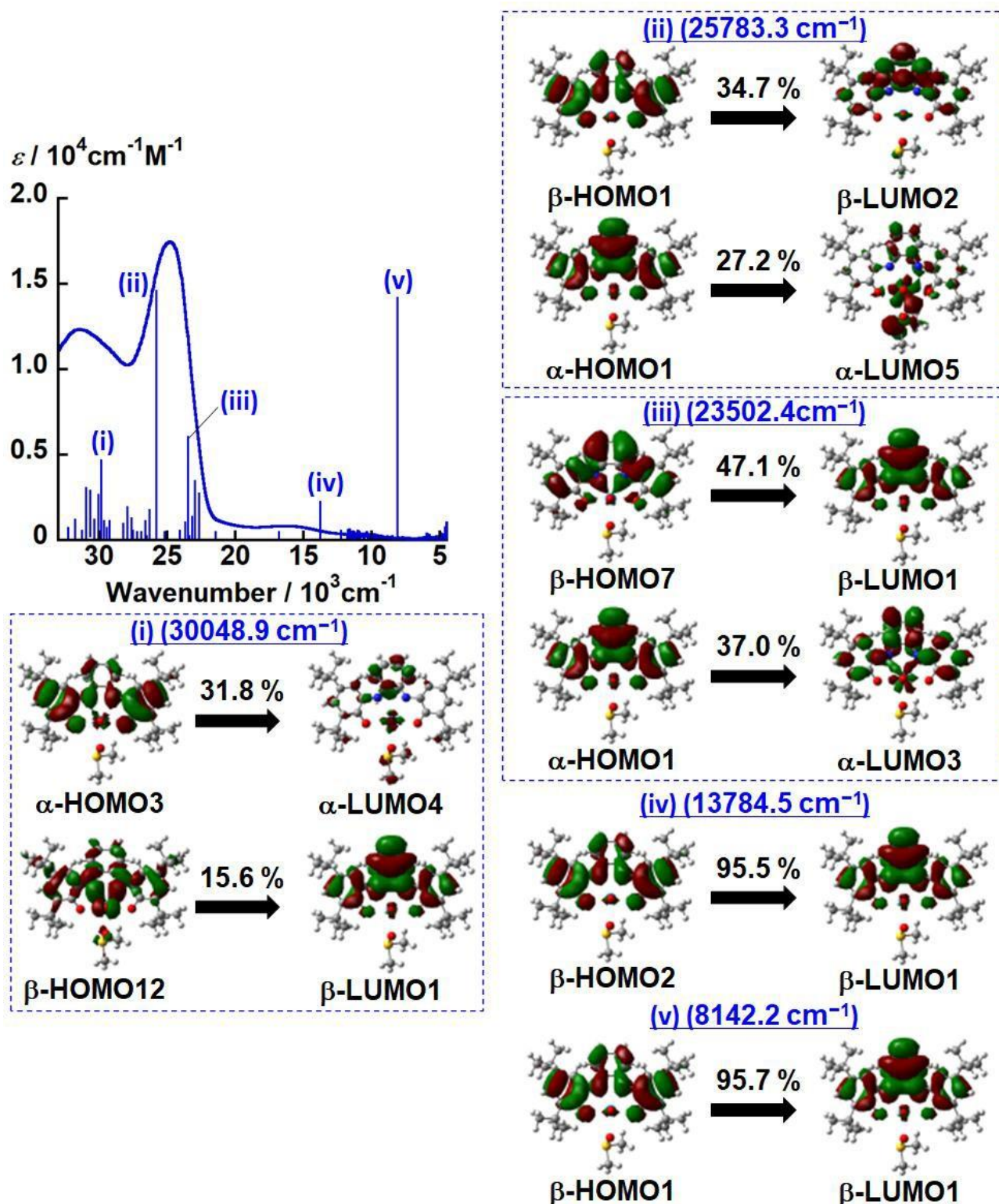**Figure S34.** Calculated MO energy diagrams of $[UO_2(L2)DMSO]^{2-}$ ($S_T = 1$).

Figure S35. UV-vis-NIR spectrum of $[UO_2(L2)DMSO]^{2-}$ in DMSO and predicted band positions and intensities of the TD-DFT calculation. The vertical blue lines correspond to the calculated transitions for $[UO_2(L2)DMSO]^{2-}$ with $S_T = 1$.

Figure S36. Calculated MO energy diagrams of $[UO_2(L3)]^{2-}$ ($S_T = 0$).

Figure S37. UV-vis-NIR spectrum of $[UO_2(L3)]^{2-}$ in DMSO and predicted band positions and intensities of the TD-DFT calculation. The vertical blue lines correspond to the calculated transitions for $[UO_2(L3)]^{2-}$ with $S_T = 0$.

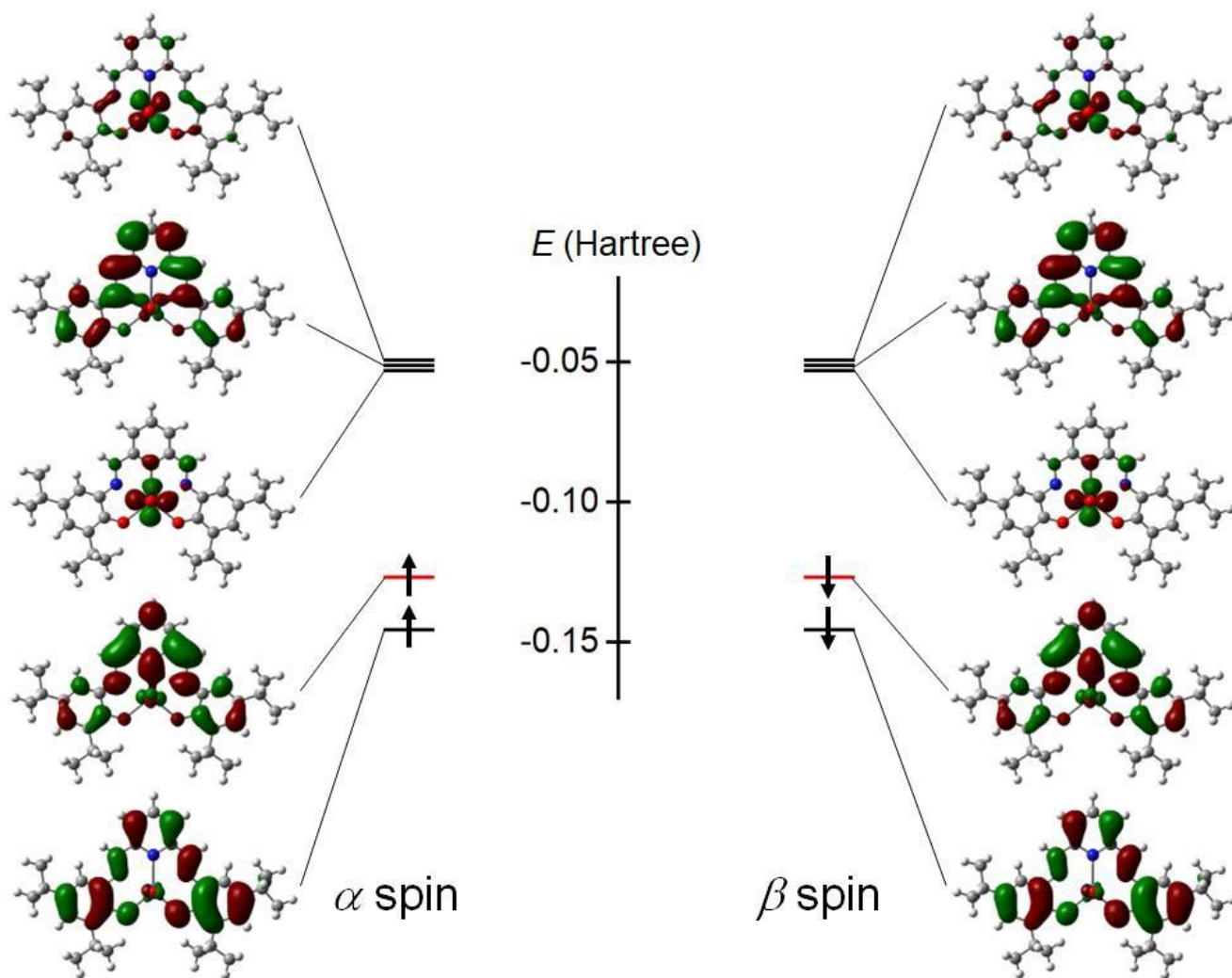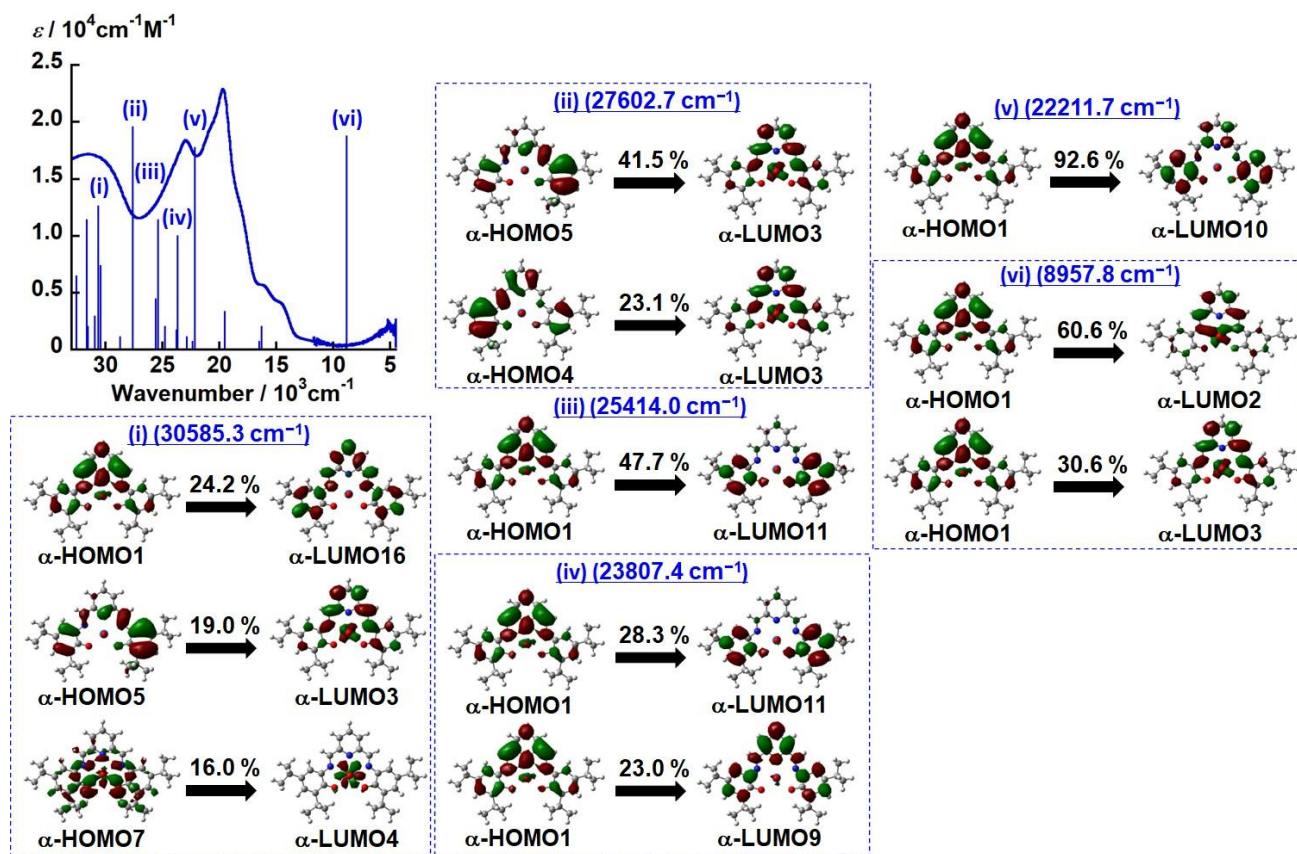**Figure S38.** Calculated MO energy diagrams of [UO$_2$(L3)]$^{2-}$ (S_T = 1).

Figure S39. UV-vis-NIR spectrum of $[UO_2(L3)]^{2-}$ in DMSO and predicted band positions and intensities of the TD-DFT calculation. The vertical blue lines correspond to the calculated transitions for $[UO_2(L3)]^{2-}$ with $S_T = 1$.
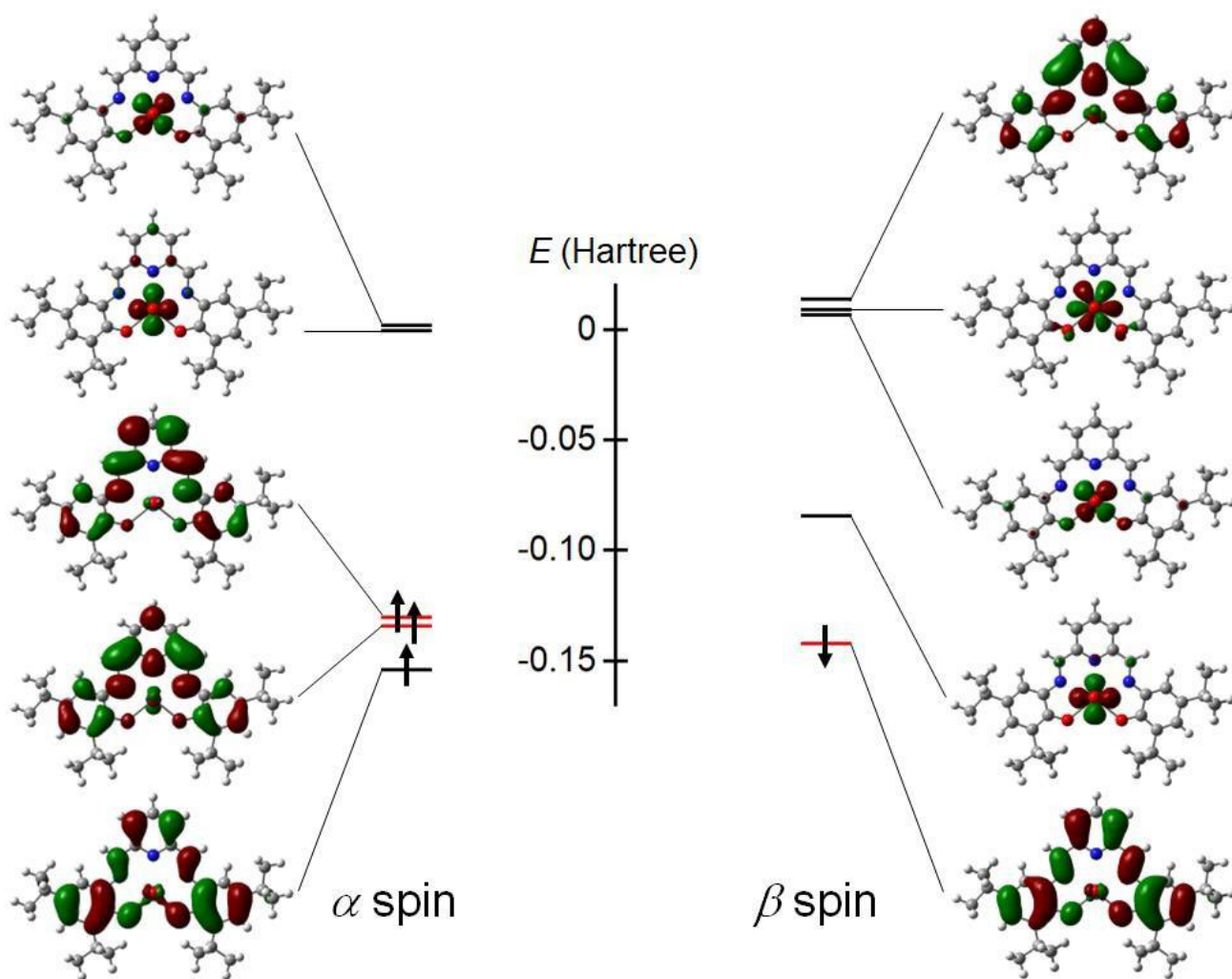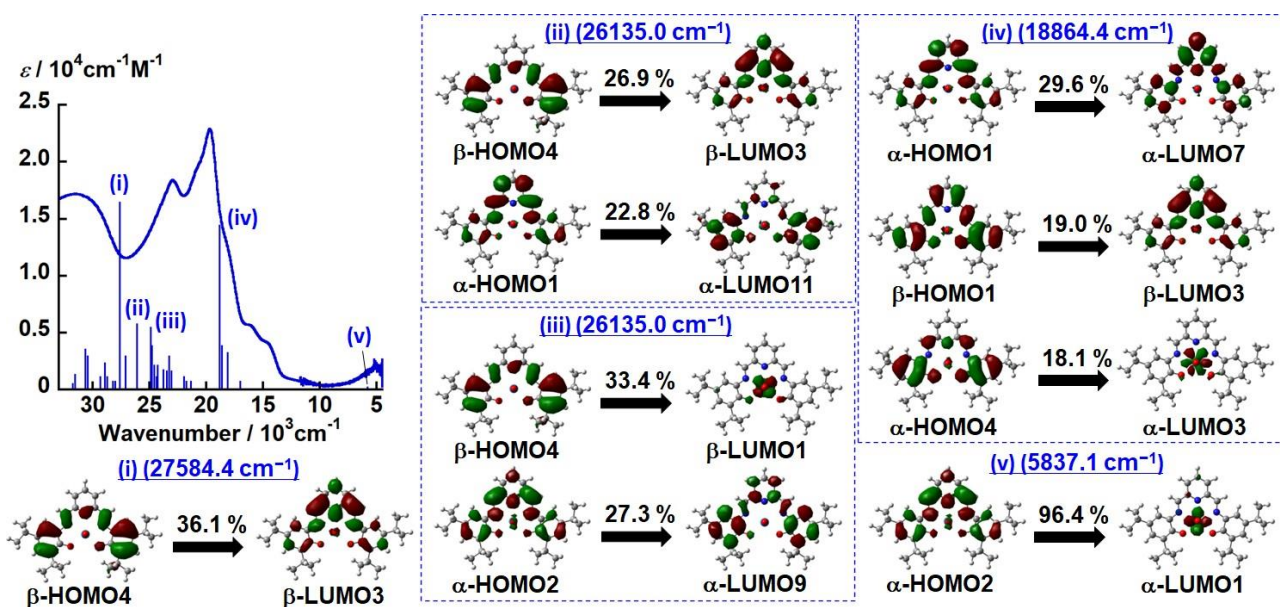
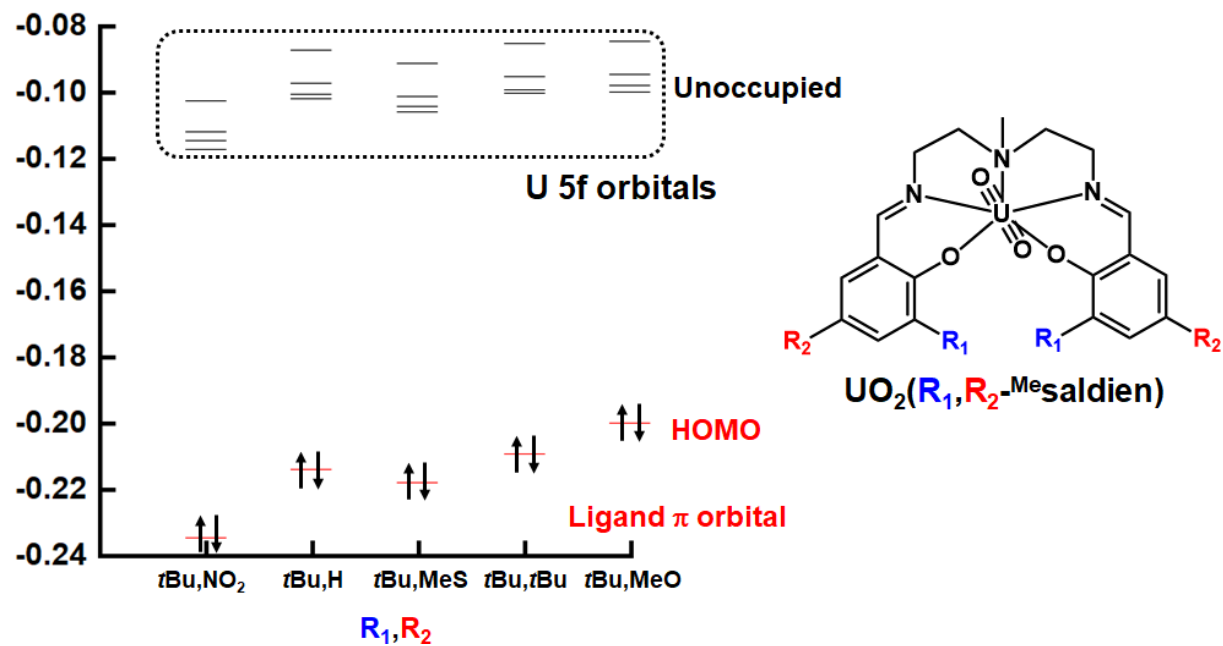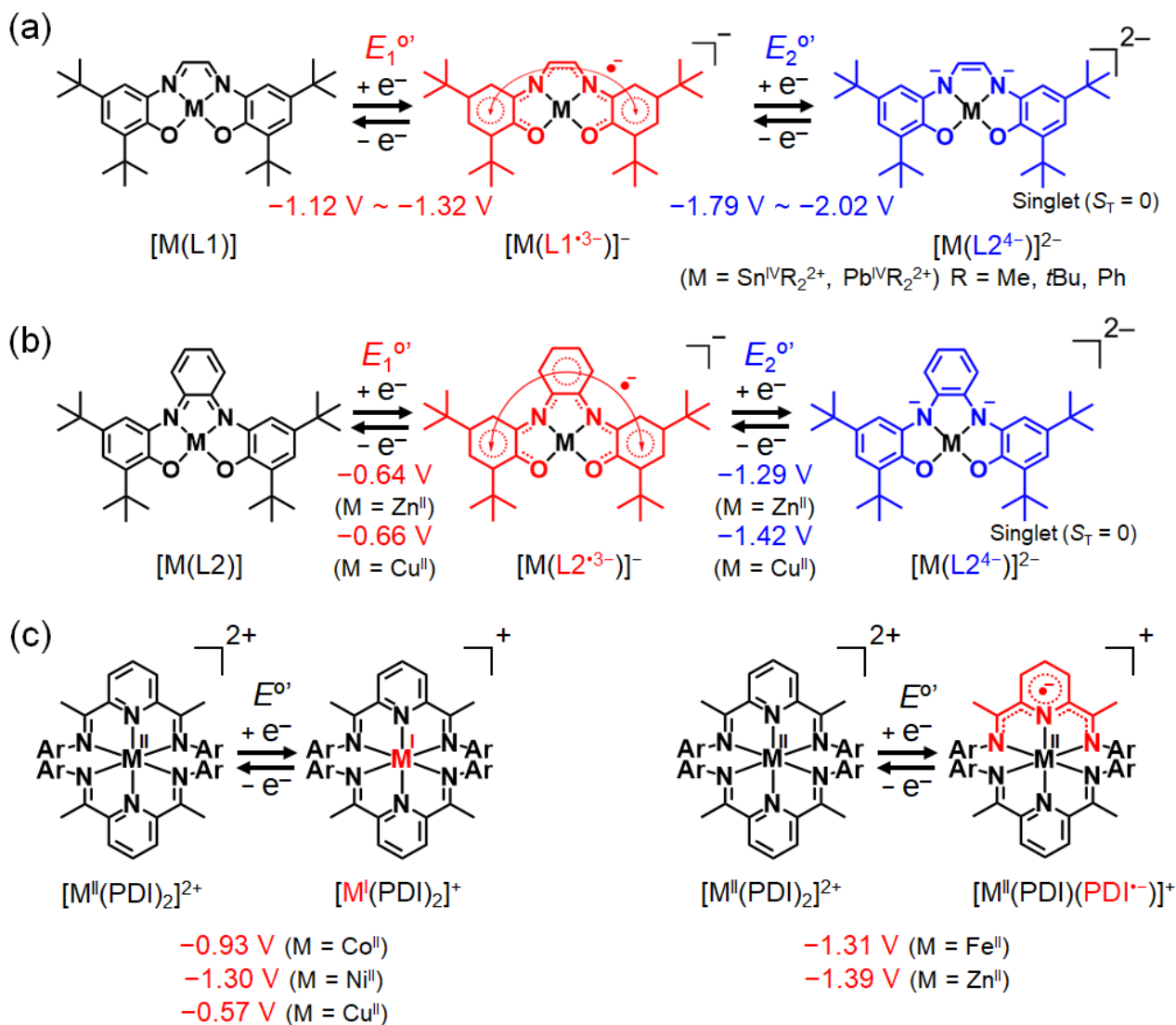**Figure S40.** Calculated MO energy diagrams of $U^{VI}O_2(R_1,R_2\text{-}^{Me}saldien)$.[S1]

(a)

$E_1^{o'}$
+ e⁻
− e⁻

−1.12 V ~ −1.32 V

$E_2^{o'}$
+ e⁻
− e⁻

Singlet ($S_T = 0$)

−1.79 V ~ −2.02 V

[M(L1)]   [M(L1$^{•3-}$)]⁻   [M(L2^{4-})]²⁻

(M = Sn^{IV}R$_2^{2+}$, Pb^{IV}R$_2^{2+}$) R = Me, tBu, Ph

(b)

$E_1^{o'}$
+ e⁻
− e⁻

−0.64 V
(M = Zn^{II})
−0.66 V
(M = Cu^{II})

$E_2^{o'}$
+ e⁻
− e⁻

−1.29 V
(M = Zn^{II})
−1.42 V
(M = Cu^{II})

Singlet ($S_T = 0$)

[M(L2)]   [M(L2$^{•3-}$)]⁻   [M(L2^{4-})]²⁻

(c)

$E^{o'}$
+ e⁻
− e⁻

[M^{II}(PDI)$_2$]²⁺   [M^I(PDI)$_2$]⁺

−0.93 V (M = Co^{II})
−1.30 V (M = Ni^{II})
−0.57 V (M = Cu^{II})

$E^{o'}$
+ e⁻
− e⁻

[M^{II}(PDI)$_2$]²⁺   [M^{II}(PDI)(PDI$^{•-}$)]⁺

−1.31 V (M = Fe^{II})
−1.39 V (M = Zn^{II})

Scheme S1. Redox behavior M(L1),[S2] M(L2)[S3] and [M^{II}(PDI)$_2$]²⁺ [S4] reported previously.

References

[S1]. T. Takeyama, S. Tsushima, K. Takao, *Inorg. Chem.*, 2021, **60**, 11435−11449.

[S2]. A. V. Piskunov, O. Y. Trofimova, G. K. Fukin, S. Y. Ketkov, I V. Smolyaninov, V. K. Cherkasov, *Dalton Trans.*, 2012, **41**, 10970−10979.

[S3]. P. Chaudhuri, M. Hess, J. Müller, K. Hildenbrand, E. Bill, T. Weyhermüller and K. Wieghardt, *J. Am. Chem. Soc.*, 1999, **121**, 9599−9610.

[S4]. B. Bruin, E. Bill, E. Bothe, T. Weyhermüller, K. Wieghardt, *Inorg. Chem.*, 2000, **39**, 2936−2947.